The Astronomical Journal, 158:54 (24pp), 2019 August https://doi.org/10.3847/1538-3881/ab2594

A Survey for New Members of Taurus from Stellar to Planetary Masses*

T. L. Esplin[1,4] and K. L. Luhman[2,3]
[1] Steward Observatory, University of Arizona, Tucson, AZ 85719, USA; taranesplin@email.arizona.edu
[2] Department of Astronomy and Astrophysics, The Pennsylvania State University, University Park, PA 16802, USA
[3] Center for Exoplanets and Habitable Worlds, The Pennsylvania State University, University Park, PA 16802, USA
Received 2019 April 15; revised 2019 May 11; accepted 2019 May 28; published 2019 July 10

Abstract

We present a large sample of new members of the Taurus star-forming region that extend from stellar to planetary masses. To identify candidate members at substellar masses, we have used color–magnitude diagrams and proper motions measured with several wide-field optical and infrared (IR) surveys. At stellar masses, we have considered the candidate members that were found in a recent analysis of high-precision astrometry from the *Gaia* mission. Using new and archival spectra, we have measured spectral types and assessed membership for these 161 candidates, 79 of which are classified as new members. Our updated census of Taurus now contains 519 known members. According to *Gaia* data, this census should be nearly complete for spectral types earlier than M6–M7 at $A_J < 1$. For a large field encompassing ∼72% of the known members, the census should be complete for $K < 15.7$ at $A_J < 1.5$, which corresponds to ∼5–13 $M_{\rm Jup}$ for ages of 1–10 Myr based on theoretical evolutionary models. Our survey has doubled the number of known members at ⩾M9 and has uncovered the faintest known member in M_K, which should have a mass of ∼3–10 $M_{\rm Jup}$ for ages of 1–10 Myr. We have used mid-IR photometry from the *Spitzer Space Telescope* and the *Wide-field Infrared Survey Explorer* to determine whether the new members exhibit excess emission that would indicate the presence of circumstellar disks. The updated disk fraction for Taurus is ∼0.7 at ⩽M3.5 and ∼0.4 at >M3.5.

Key words: brown dwarfs – protoplanetary disks – stars: low-mass – stars: formation

Supporting material: data behind figures, machine-readable tables

1. Introduction

The Taurus cloud complex is one of the nearest star-forming regions ($d \sim 140$ pc, Galli et al. 2018, references therein) and has a relatively large stellar population ($N \sim 500$; Kenyon et al. 2008; this work), making it well suited for studies of star formation that reach low stellar masses and have good statistics. In addition, Taurus has an unusually low stellar density compared to other nearby molecular clouds, so it can help constrain how the star formation process depends on environment. However, a complete census of Taurus is challenging given that its members are distributed across a large area of sky (∼100 deg^2).

Surveys for members of Taurus have steadily improved in sensitivity and areal coverage over the past 30 years (Kraus et al. 2017; Luhman et al. 2017, references therein). We have recently sought to advance this work in Esplin & Luhman (2017) and Luhman (2018). In the first survey, we searched for members down to planetary masses (<15 $M_{\rm Jup}$) across a large fraction of Taurus using optical and infrared (IR) imaging from the *Spitzer Space Telescope* (Werner et al. 2004), the United Kingdom Infrared Telescope (UKIRT) Infrared Deep Sky Survey (UKIDSS; Lawrence et al. 2007), Pan-STARRS1 (PS1; Kaiser et al. 2002, 2010), and the *Wide-field Infrared Survey Explorer* (*WISE*; Wright et al. 2010). Meanwhile, Luhman (2018) used high-precision astrometry and optical photometry from the second data release (DR2) of the *Gaia* mission (Perryman et al. 2001; de Bruijne 2012; Gaia Collaboration et al. 2016b, 2018) to perform a thorough census of stellar members with low-to-moderate extinctions across the entire cloud complex.

We have continued the survey for low-mass brown dwarfs in Taurus from Esplin et al. (2018) by including new IR imaging from UKIRT and the Canada–France–Hawaii Telescope (CFHT). We also have obtained spectra of most of the candidate stellar members that were identified with *Gaia* by Luhman (2018). In this paper, we update the catalog of known members of Taurus from Luhman (2018) (Section 2); identify candidate members using photometry, proper motions, and parallaxes (Sections 3 and 4); and spectroscopically classify the candidates (Section 5). We assess the new members for evidence of circumstellar disks and estimate the disk fraction as a function of stellar mass among the known members (Section 6). We conclude by using our new census of Taurus to constrain the region's initial mass function (IMF), particularly at the lowest masses (Section 7).

2. Catalog of Known Members of Taurus

For our census of Taurus, we begin with the 438 objects adopted as members by Luhman (2018), which were vetted for contaminants using the proper motions and parallaxes from *Gaia* DR2. In that catalog, the components of a given multiple system appeared as a single entry if they were unresolved by *Gaia* and the imaging data utilized by Esplin & Luhman (2017). Luhman (2018) overlooked the fact that HK Tau B and V1195 Tau B were resolved from their primaries by *Gaia*. They are now given separate entries in our census. We also adopt 2MASS J04282999 +2358482 as a member, which was discovered to be a young late M object by Gizis et al. (1999). It satisfies our photometric and astrometric criteria for membership and is located near other known members. We exclude from our membership list one of the

* Based on observations made with the NASA Infrared Telescope Facility, Gemini Observatory, UKIRT, MMT, CFHT, Pan-STARRS1, 2MASS, UKIDSS, UHS, SDSS, *Gaia*, *WISE*, and the *Spitzer Space Telescope*, which is operated by the Jet Propulsion Laboratory, California Institute of Technology, under a contract with NASA.
[4] Strittmatter Fellow.

Table 1
Members of Taurus

Column Label	Description
2MASS	2MASS Point Source Catalog source name
UGCS	UKIDSS Galactic Clusters Survey source name[a]
Gaia	*Gaia* DR2 source name
Name	Other source name
RAdeg	R.A. (J2000)
DEdeg	decl. (J2000)
Ref-Pos	Reference for R.A. and decl.[b]
SpType	Adopted spectral type[c]
GaiapmRA	Proper motion in R.A. from *Gaia* DR2
e_GaiapmRA	Error in GaiapmRA
GaiapmDec	Proper motion in decl. from *Gaia* DR2
e_GaiapmDec	Error in GaiapmDec
plx	Parallax from *Gaia* DR2
e_plx	Error in plx
f_plx	Flag on parallax[d]
Gmag	G magnitude from *Gaia* DR2
e_Gmag	Error in Gmag
GBPmag	G_{BP} magnitude from *Gaia* DR2
e_GBPmag	Error in GBPmag
GRPmag	G_{RP} magnitude from *Gaia* DR2
e_GRPmag	Error in GRPmag
RUWE	Renormalized unit weight error from Lindegren (2018)
Pop	Population from Luhman (2018)
IRpmRA	Proper motion in R.A. from 2MASS/WFCAM/IRAC
e_IRpmRA	Error in IRpmRA
IRpmDec	Proper motion in decl. from 2MASS/WFCAM/IRAC
e_IRpmDec	Error in IRpmDec
Jmag	J magnitude
e_Jmag	Error in Jmag
r_Jmag	Reference for Jmag[e]
Hmag	H magnitude
e_Hmag	Error in Hmag
r_Hmag	Reference for Hmag[e]
Kmag	K or K_s magnitude
e_Kmag	Error in Kmag
r_Kmag	Reference for Kmag[e]
3.8mag	*Spitzer* [3.6] band magnitude
e_3.6mag	Error in 3.6mag
f_3.6mag	Flag on 3.6mag[f]
4.5mag	*Spitzer* [4.5] band magnitude
e_4.5mag	Error in 4.5mag
f_4.5mag	Flag on 4.5mag[f]
5.8mag	*Spitzer* [5.8] band magnitude
e_5.8mag	Error in 5.8mag
f_5.8mag	Flag on 5.8mag[f]
8.0mag	*Spitzer* [8.0] band magnitude
e_8.0mag	Error in 8.0mag
f_8.0mag	Flag on 8.0mag[f]
24mag	*Spitzer* [24] band magnitude
e_24mag	Error in 24mag
Ref-Spitz	Reference for *Spitzer* photometry[g]
f_24mag	Flag on 24mag[f]
W1mag	*WISE W1* band magnitude
e_W1mag	Error in W1mag
f_W1mag	Flag on W1mag[f]
W2mag	*WISE W2* band magnitude
e_W2mag	Error in W2mag
f_W2mag	Flag on W2mag[f]
W3mag	*WISE W3* band magnitude
e_W3mag	Error in W3mag
f_W3mag	Flag on W3mag[f]
W4mag	*WISE W4* band magnitude
e_W4mag	Error in W4mag
f_W4mag	Flag on W4mag[f]
Exc4.5	Excess present in [4.5]?
Exc8.0	Excess present in [8.0]?
Exc24	Excess present in [24]?
ExcW2	Excess present in *W2*?
ExcW3	Excess present in *W3*?
ExcW4	Excess present in *W4*?
DiskType	Disk type[h]
Aj	Extinction in J
f_Aj	Method for estimating extinction in J[i]

Notes.
[a] Based on coordinates from data release 10 of the UKIDSS Galactic Clusters Survey for stars with $K_s > 10$ from 2MASS.
[b] Sources of the R.A. and decl. are are the 2MASS Point Source Catalog, Gaia DR2, UKIDSS data release 10, and images from the *Spitzer Space Telescope* (Luhman et al. 2010).
[c] Spectral types adopted by Luhman et al. (2017), Esplin & Luhman (2017), and Luhman (2018) for previously known members and types measured in this work for new members (Table 4).
[d] * = Discrepant parallax relative to other members of Taurus, as noted in Luhman (2018) and the Appendix.
[e] 1 = 2MASS Point Source Catalog; 2 = UKIRT Hemisphere Survey; 3 = UKIDSS data release 10; 4 = our UKIRT photometry (Section 3.1.3); 5 = WIRCam photometry.
[f] nodet = non-detection; sat = saturated; out = outside of the camera's field of view; bl = photometry may be affected by blending with a nearby star; bin = includes an unresolved binary companion; unres = too close to a brighter star to be detected; false = detection from *WISE* catalog appears false or unreliable based on visual inspection.
[g] 1 = Luhman et al. (2010); 2 = Esplin et al. (2014); 3 = Esplin & Luhman (2017); 4 = this work.
[h] From Luhman et al. (2010), Esplin et al. (2014), Esplin & Luhman (2017), and this work.
[i] $J - H$ and $J - K_s$ = derived from these colors assuming photospheric near-IR colors (Luhman et al. 2010); CTTS = derived from $J - H$ and $H - K_s$ colors assuming intrinsic colors of classical T Tauri stars from Meyer et al. (1997); opt spec = derived from an optical spectrum; IR spec = derived from an infrared spectrum; 1 = Briceño et al. (1998); 2 = Luhman (1999b); 3 = Strom & Strom (1994); 4 = Beck (2007); 5 = White & Ghez (2001); 6 = DeWarf et al. (2003); 7 = Calvet et al. (2004).

(This table is available in its entirety in machine-readable form.)

stars from Luhman (2018), 2MASS 05023985+2459337, for reasons discussed in the Appendix. When the 79 new members from our survey are included (Section 5), we arrive at a catalog of 519 known members of Taurus, which are presented in Table 1. That tabulation contains adopted spectral types, astrometry and photometry from *Gaia* DR2 and the corresponding kinematic populations from Luhman (2018), proper motions measured in Section 3.3, near-IR photometry from various sources, mid-IR photometry from *Spitzer* and *WISE* and the resulting disk classifications (Luhman et al. 2010; Esplin et al. 2014; Esplin & Luhman 2017, Section 6), and extinction estimates. For each star that appears in *Gaia* DR2, we also list the value of the renormalized unit weight error (RUWE; Lindegren 2018), which indicates the quality of the astrometric fit (Section 4). Luhman (2018) compiled available radial velocity measurements for known members of Taurus and calculated *UVW* velocities from the combination of those radial velocities and the *Gaia* proper

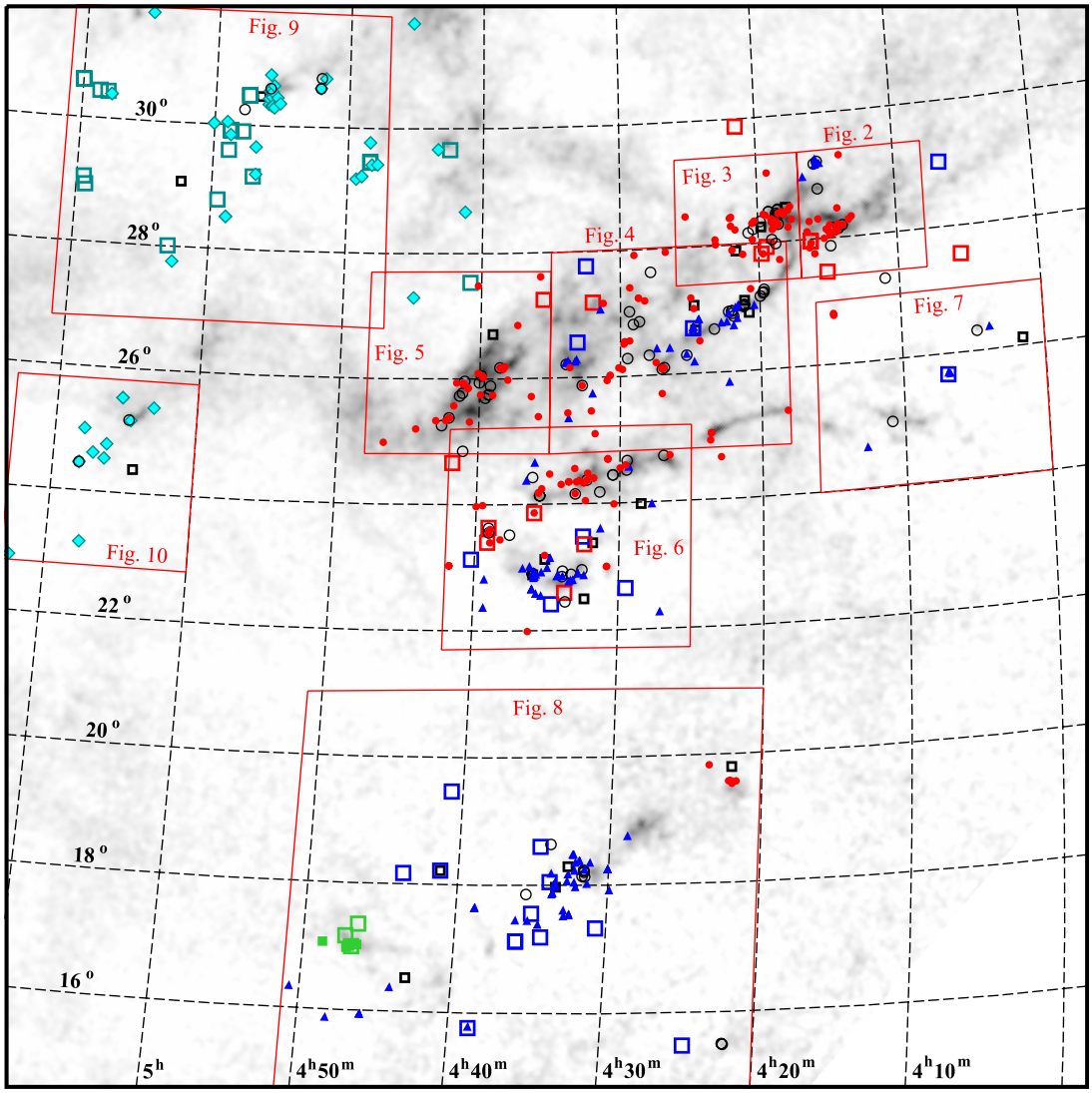

Figure 1. Spatial distribution of the known members of Taurus. Previously known members with parallaxes and proper motions from *Gaia* DR2 are shown with filled symbols (red circles, blue triangles, green squares, cyan diamonds), and previous members that lack *Gaia* data are plotted with black open circles. The colors of the filled symbols correspond to the kinematic populations from Luhman (2018). New members from this work are plotted with open squares that follow the same color scheme. The boundaries of the fields encompassed by Figures 2–10 are marked by the red rectangles. The dark clouds in Taurus are displayed with a map of extinction (gray scale; Dobashi et al. 2005).

motions and parallaxes. Two of the new members from our survey, *Gaia* 146708734143437568 and 152104381299305856, also have radial velocity measurements (16.6 ± 0.8 km s^{-1}, 17.5 ± 1.6 km s^{-1}), both of which are from *Gaia* DR2.

A map of the spatial distribution of the members is shown in Figure 1. Kinematic and photometric data for the members within nine fields that cover subsections of Taurus are plotted in Figures 2–10, which contain diagrams from Luhman (2018) that have been updated to include the new members from this work. The boundaries for those fields are indicated in Figure 1.

3. Identification of Candidate Members at Substellar Masses

3.1. Photometry and Astrometry

3.1.1. Data Utilized by Esplin & Luhman (2017)

In Esplin & Luhman (2017), we identified candidate substellar members of Taurus based on their proper motions and positions in color–magnitude diagrams (CMDs). We considered astrometry and photometry for objects within a field encompassing all of the Taurus clouds ($\alpha = 4^{\rm h}$–$5^{\rm h}10^{\rm m}$, $\delta = 15°$–$31°$) in several optical and IR bands: JHK_s from the Point Source Catalog of the Two Micron All Sky Survey (2MASS; Skrutskie et al. 2006; Cutri et al. 2013); bands at 3.6, 4.5, 5.8, and 8.0 μm ([3.6], [4.5], [5.8], [8.0]) from the Infrared Array Camera (IRAC; Fazio et al. 2004) on the *Spitzer Space Telescope* (Werner et al. 2004); *ZYJHK* from data release 10 of UKIDSS; $rizy_{P1}$ from the first data release of PS1 (Chambers et al. 2016; Flewelling et al. 2016); *riz* from data release 13 of the Sloan Digital Sky Survey (SDSS; York et al. 2000; Finkbeiner et al. 2004; Albareti et al. 2017); *G* from the first data release of *Gaia* (Gaia Collaboration et al. 2016a, 2016b); and bands at 3.5, 4.6, 12, and 22 μm (*W*1, *W*2, *W*3, *W*4) from the AllWISE Source Catalog. The extinction for each object was estimated using $J - H$ and $J - K_s$ colors, and it was used to deredden the photometry in the CMDs with reddening relations from Indebetouw et al. (2005), Schlafly et al. (2016),

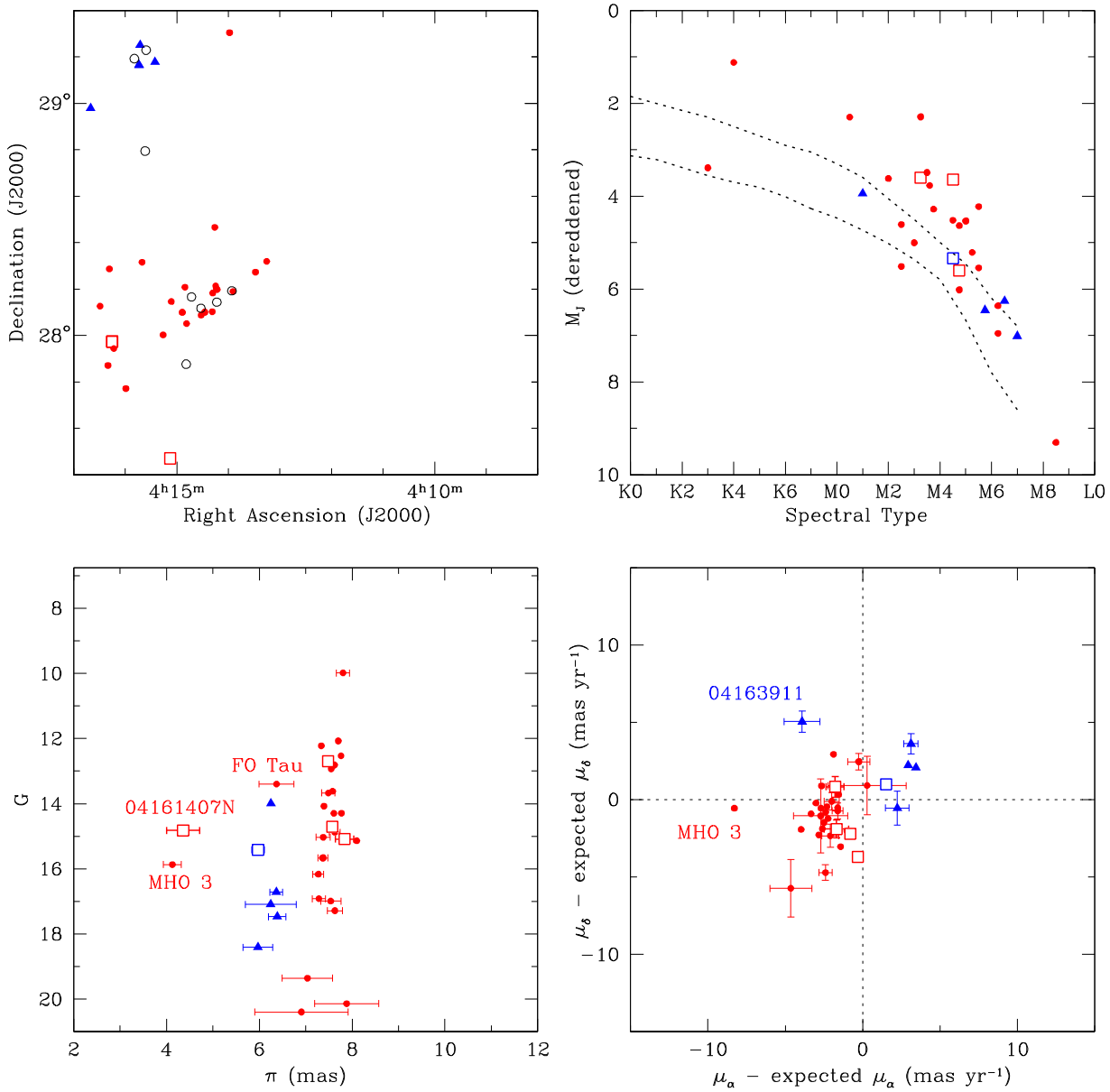

Figure 2. Diagrams of spatial distribution, extinction-corrected M_J vs. spectral type, G vs. parallax, and proper motion offsets for previously known members of Taurus and new members from this work that are projected against the B209 cloud. The latter three diagrams consist of stars that have parallaxes and proper motions from *Gaia* DR2. The symbols are the same as in Figure 1. The diagram of M_J vs. spectral type includes the median sequences for Taurus and Upper Sco (upper and lower dotted lines). The latter has an age of ∼11 Myr (Pecaut et al. 2012; Feiden 2016). The proper motion offsets are relative to the values expected for the positions and parallaxes of the stars assuming the median space velocity of Taurus members (Luhman 2018). In the bottom panels, errors are not plotted when they are smaller than the symbols (<0.1 mas, <0.5 mas yr^{-1}). Stars with discrepant parallaxes and proper motions are labeled (Luhman 2018, Appendix).

and Xue et al. (2016). We measured relative proper motions between 2MASS and *Gaia* DR1, between 2MASS and PS1, and across several epochs of IRAC imaging. Relative motions from UKIDSS were also employed. 2MASS, *WISE*, and PS1 provided data for the entirety of our survey field, while *Spitzer*, SDSS, and UKIDSS covered a subset of it (Esplin & Luhman 2017; Luhman et al. 2017). The fields observed by IRAC are indicated in Figure 11.

3.1.2. UHS

New J-band photometry has become available in Taurus through the first data release of the UKIRT Hemisphere Survey (UHS; Dye et al. 2018). Those data were taken with UKIRT's Wide Field Camera (WFCAM; Casali et al. 2001), which also was used for UKIDSS. UHS provides J photometry for a large portion of Taurus that was not observed by UKIDSS in that band. We have adopted the 1″ aperture photometry from UHS, which has a similar completeness limit to the data from UKIDSS ($J \sim 18.5$).

3.1.3. UKIRT

UKIDSS has imaged most of Taurus in K and roughly half of it in ZYJ. Only a small portion of Taurus was observed in H. When combined with J and an optical band, H is particularly useful for distinguishing late-type members from reddened background stars. To improve the coverage of Taurus in H and the other bands, we have obtained new images with WFCAM at UKIRT. The observations were similar to those from UHS

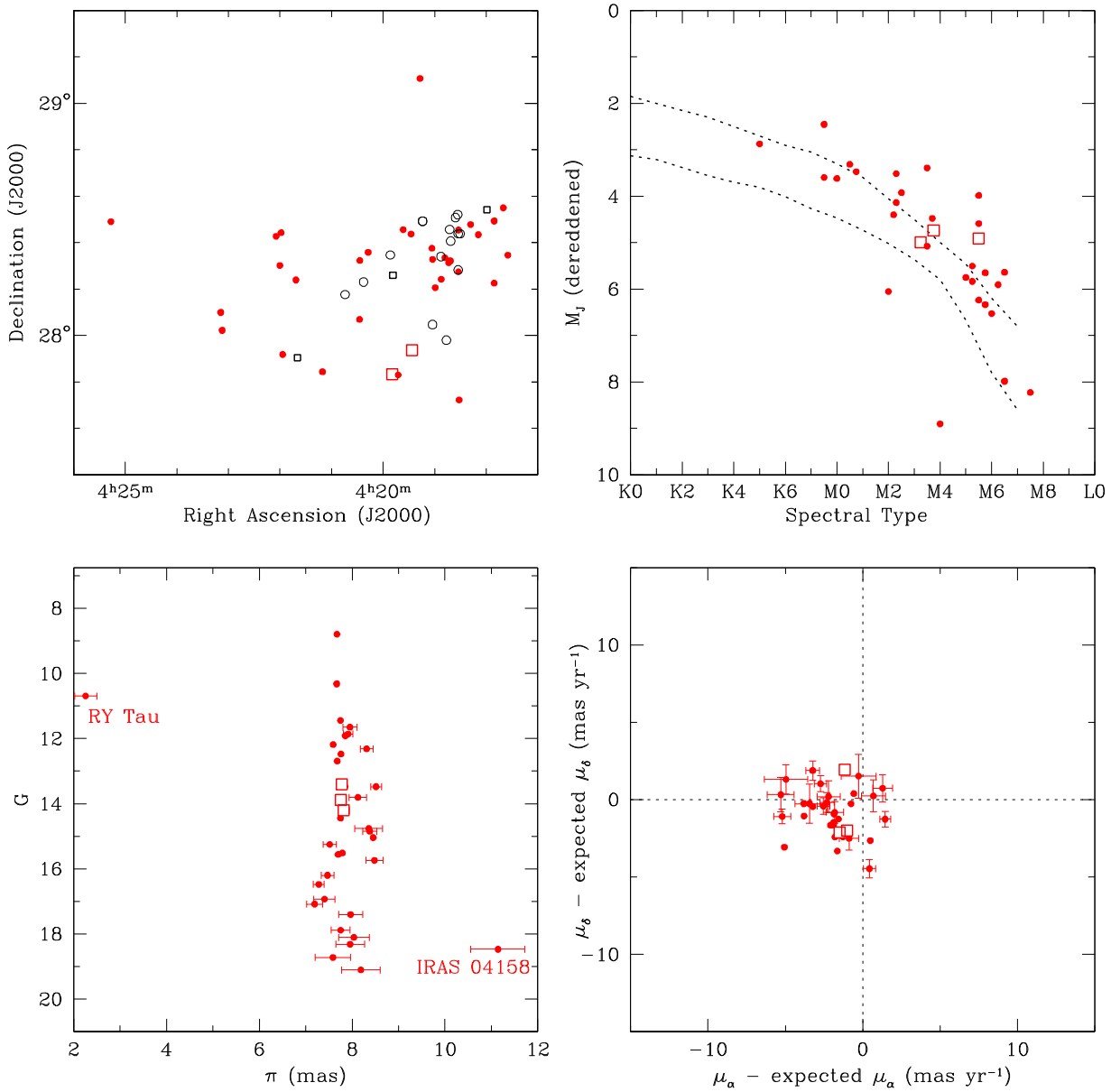

Figure 3. Same as Figure 2, but for members projected against the L1495 cloud.

and UKIDSS, consisting of 3 × 15 s exposures in *Y* and 4 × 10 s exposures in *JHK* at each position. The data were collected between 2017 September and December. In Figure 11, we show the fields that now have *JHK* photometry from WFCAM through UKIDSS, UHS, and our observations.

The initial data reduction steps (e.g., flat-fielding, registration, co-addition) were performed by the WFCAM pipeline (Irwin et al. 2004; Hambly et al. 2008). We derived the flux calibration for the resulting images using photometry from previous surveys (e.g., PS1, 2MASS). The typical values of FWHM for point sources in the images were 1.″1 for *Y* and 0.″8 for *JHK*. We identified sources in the pipeline images and measured aperture photometry for them using the routines `starfind` and `phot` in IRAF. We estimated the completeness limits of the data based on the magnitudes at which the logarithm of the number of stars as a function of magnitudes deviates from a linear slope and begins to decline, which were 18.5, 17.5, and 17.2 for *J*, *H*, and *K*, respectively. Similar limits are exhibited by the UKIDSS data in Taurus. Our *Y* data have a completeness limit near 18.5, which is ∼0.5 mag brighter than the value for UKIDSS.

3.1.4. CFHT

Near-IR images of portions of Taurus are publicly available from the archive of CFHT. We have utilized the data taken in *J*, *H*, and a narrowband filter at 1.45 μm (*W*) with the Wide-field Infrared Camera (WIRCam) through programs 15BC11, 16AC13, 16BC17 (E. Artigau), 15BT11 (W.-P. Chen), 16AF16, 16BF22 (M. Bonnefoy), and 16AT04 (P. Chiang). For most of the observations, individual exposure times were 10, 10, and 65 s for *J*, *H*, and *W*, respectively, and the number of exposures per field was 4–8. Point sources in the images typically exhibited FWHM ∼ 0.″6–0.″8. We began our analysis with the images from the CFHT archive that had been pipeline processed (e.g., flat-fielding, dark subtraction, bad pixel masking). We registered and combined the images for a given field and filter. For the resulting mosaics, we derived the

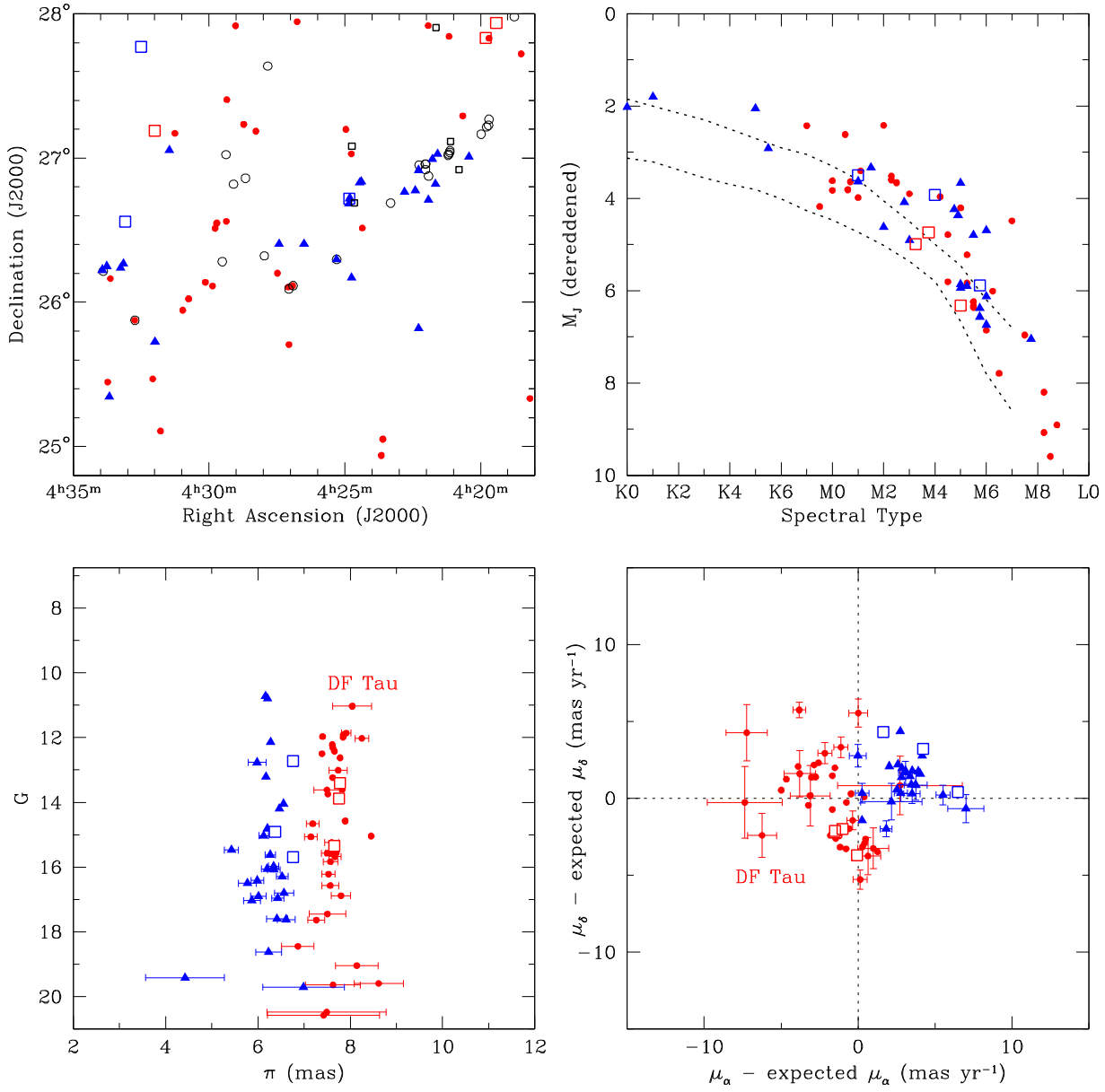

Figure 4. Same as Figure 2, but for members projected against the L1521, B213, and B215 clouds.

astrometric and flux calibrations with data from 2MASS and UKIDSS. Since W is a custom filter that is absent from 2MASS and UKIDSS, we calibrated the relative photometry among different W images such that their loci of reddened stars in $W - H$ versus $J - H$ were aligned with each other. Relative photometry of this kind in W is sufficient for our purposes of identifying late-type objects based on colors. We identified sources in the images and measured their aperture photometry with `starfind` and `phot` in IRAF. The completeness limits for these data are $J = 18.2$, $W = 18.0$, and $H = 17.5$. The fields covered by WIRCam are indicated in Figure 11.

3.2. Color–Magnitude Diagrams

We have identified all matching sources among our new catalogs and those considered by Esplin & Luhman (2017). When multiple measurements in similar bands were available for a star, we selected the data to adopt in the manner described by Esplin & Luhman (2017). We omitted photometry with errors >0.15 mag in Y and >0.1 mag in the other bands. In Esplin & Luhman (2017), we constructed diagrams of K_s (or K) versus $G - K_s$, $r - K_s$, $i - K_s$, $z_{P1} - K_s$, $Z - K_s$, $y_{P1} - K_s$, $Y - K_s$, $H - K_s$, $K_s -$ [3.6], and $K_s - W1$. We also included a diagram of $W1$ versus $W1 - W2$. As explained in that study, we estimated the extinction for individual stars from $J - H$ and $J - K_s$ and dereddened the photometry in most of the CMDs. In each CMD, we marked a boundary that followed the lower envelope of the sequence of known members. Objects appearing above any of those boundaries and not appearing below any of them were treated as candidate members. We have applied those CMDs to our updated compilation of photometry. Four examples of the CMDs are presented in Figure 12. In addition, we show a diagram that makes use of the W-band data from WIRCam, $W - H$ versus $J - W$. The W filter falls within a steam absorption band, while J and H encompass continuum on either side of the band, so the combination of $J - W$ and $W - H$ can be used to identify late-type objects via their strong steam

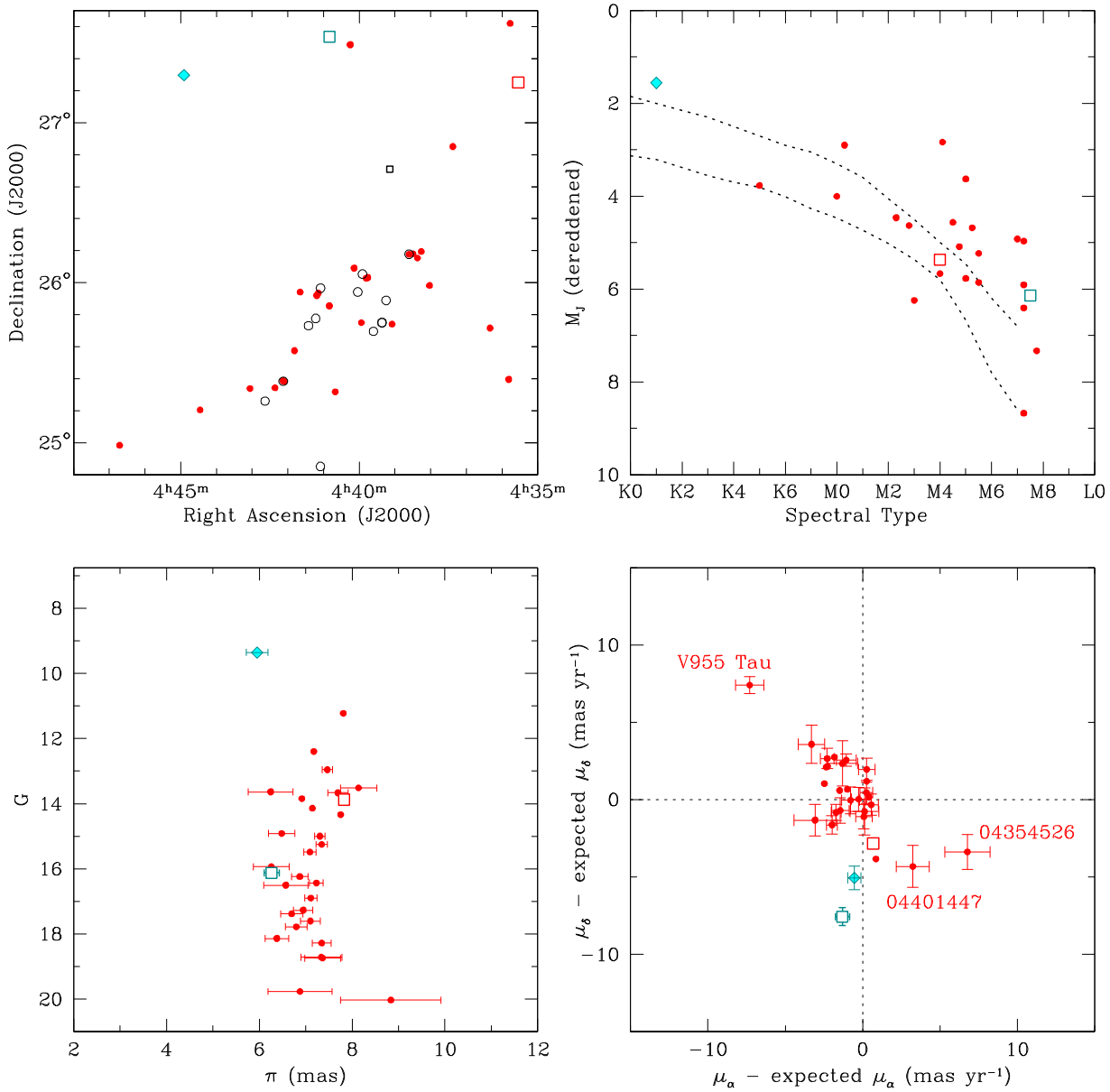

Figure 5. Same as Figure 2, but for members projected against the L1527 cloud.

absorption. In the diagram of those colors, we have plotted a reddening vector near the lower edge of the population of known members later than M6. Objects above that vector are treated as late-type candidates as long as they are not rejected by any other diagrams. We note that many of the known <M6 members of Taurus within the WIRcam images are saturated and hence are absent from the diagram of $W - H$ versus $J - W$.

3.3. Proper Motions

As mentioned in Section 3.1.1, Esplin & Luhman (2017) measured proper motions in Taurus with astrometry from 2MASS, PS1, *Gaia* DR1, and IRAC. In addition to those data, we have made use of new motions measured from a combination of 2MASS, IRAC, UKIDSS, UHS, and our new WFCAM data, which have epochs spanning 20 years. The latter four sets of data, which are deeper than 2MASS, span 13 years and reach the lowest masses in Taurus among the available motions. To measure the proper motions, we began by aligning each set of astrometry to the *Gaia* DR2 reference frame. Motions were then computed with a linear fit to the available astrometry. In Figure 13, we show the resulting motions for individual known members of Taurus and for other sources projected against Taurus, which are represented by density contours. The measurements for the known members have typical errors of ∼2–3 mas yr^{-1}. Motions with errors of >10 mas yr^{-1} are ignored. As done with the other catalogs of proper motions in Esplin & Luhman (2017), we have identified candidate members based on motions that have 1σ errors overlapping with a radius of 10 mas yr^{-1} from the median motion of the known members (Figure 13). Six known members of Taurus do not satisfy this threshold, three of which have *Gaia* DR2 motions that are consistent with membership (Luhman 2018). The remaining three sources are 2MASS J04355209+2255039, J04354526+2737130, and J04574903+3015195. The first two objects also have

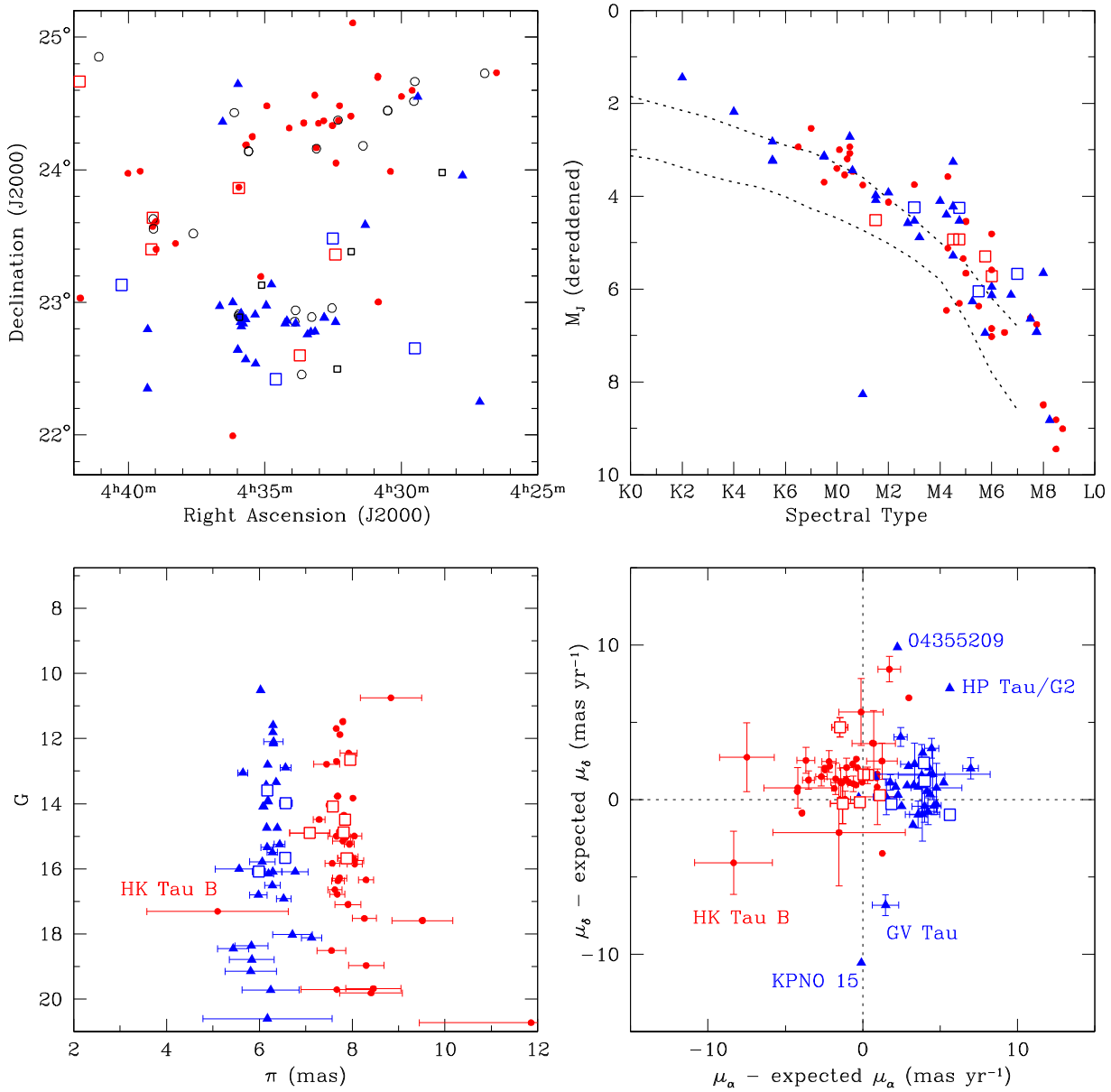

Figure 6. Same as Figure 2, but for members projected against the L1524, L1529, and L1536 clouds.

discrepant motions in *Gaia* DR2 but are retained as members for reasons discussed by Luhman (2018). The third star is retained as a member since it is near known members and is only slightly beyond our proper motion threshold.

4. Identification of Candidate Members at Stellar Masses

Gaia DR2 provides high-precision astrometry at an unprecedented depth for a wide-field survey. For stars at $G \lesssim 20$, the *Gaia* parallaxes and proper motions have typical errors of $\lesssim$0.7 mas and $\lesssim$1.2 mas yr^{-1}, respectively (Gaia Collaboration et al. 2018), which correspond to errors of $\lesssim$10% and $\lesssim$5%, respectively, for unreddened members of Taurus at masses of $\gtrsim$0.05 $M_{\odot}$. As a result, *Gaia* DR2 enables the precise kinematic identification of members of Taurus at stellar masses.

Luhman (2018) selected stars from *Gaia* DR2 that have proper motions and parallaxes that are similar to those of the known members of Taurus. In that analysis, the parameters `astrometric_gof_al` and `astrometric_excess_noise` from *Gaia* DR2 were used to identify stars with poor astrometric fits and hence potentially unreliable astrometry. More recently, Lindegren (2018) has presented a new parameter, RUWE, that serves as a better indicator of the goodness of fit. He found that the distribution of RUWE in *Gaia* DR2 exhibited a break near 1.4 between the distribution centered at unity expected for well-behaved fits and a long tail to higher values. Thus, RUWE $\lesssim$ 1.4 could be adopted as a criterion for reliable astrometry. To illustrate the application of this threshold to Taurus, we plot in Figure 14 the distribution of log(RUWE) for known members (including the new ones from this work) that have parallaxes and proper motions from *Gaia* DR2. We also indicate the subset of members that are noted in Luhman (2018) and the Appendix as having discrepant parallaxes (Table 1). The latter distribution does begin just above the threshold of 1.4 from Lindegren (2018), supporting its applicability to Taurus. Above that threshold, the fraction of members with discrepant astrometry increases with higher values of RUWE. Most members with RUWE >1.4 do not have

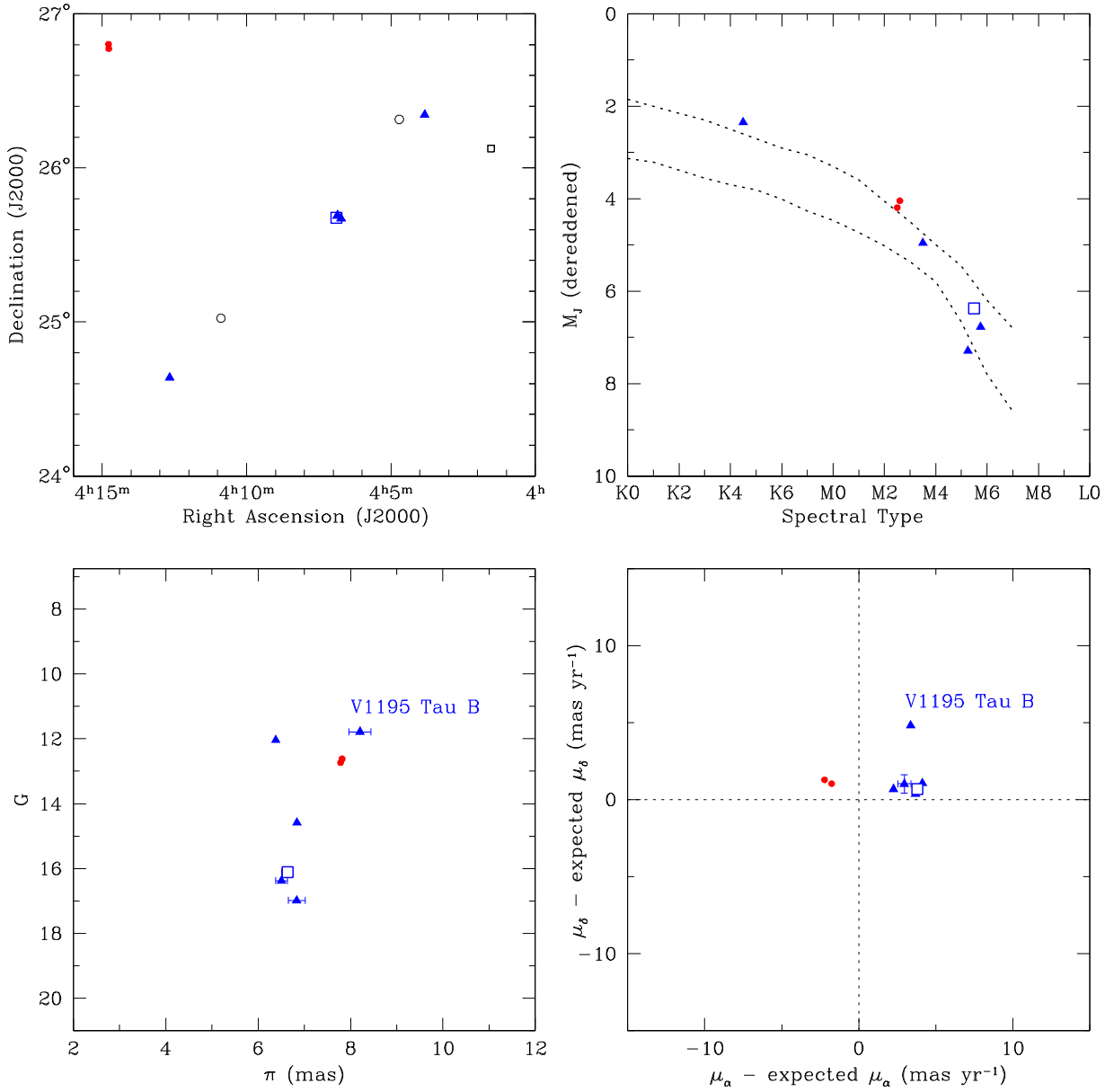

Figure 7. Same as Figure 2, but for members projected against the L1489 and L1498 clouds.

discrepant astrometry, indicating that many stars with high RUWE have fits that are sufficiently good for useful astrometry.

The selection criteria from Luhman (2018) produced a sample of 62 candidate members of Taurus. Most of the candidates should have spectral types of M2–M6 based on their colors. In the next section, we present spectroscopic classifications for 61 of those stars, 54 of which are adopted as members. The one remaining candidate that lacks a spectrum is *Gaia* 157816859599833472. It is located 6″ from a much brighter star, HD 30111. The two stars have similar proper motions, but the parallax of HD 30111 (3.0 ± 0.2 mas) is much smaller than those of Taurus members (6–8 mas), so it was not selected as a candidate member. However, the value of RUWE for HD 30111 is high enough (2.4) to indicate a poor astrometric fit and potentially unreliable astrometry. Therefore, based on its proximity to the candidate *Gaia* 157816859599833472 and its similar motion, we treat HD 30111 as a candidate member.

Luhman (2018) noted three stars that did not satisfy the selection criteria for candidates but were located within a few arcseconds of candidates and hence could be companions to them. They consist of *Gaia* 164475467659453056, *Gaia* 3314526695839460352, and *Gaia* 3409647203400743552. We present spectral classifications for those stars in the next section.

We have searched for additional companions that were detected by *Gaia* but were not identified as candidate members by Luhman (2018). We began by retrieving all sources from *Gaia* DR2 that are within 5″ from known Taurus members. We omitted companions or candidate companions that were already known and stars that appear below the sequence of Taurus members in CMDs of *Gaia* photometry. The remaining sample consists of *Gaia* 152416436441091584, *Gaia* 3415706130-945884416, *Gaia* 148400225409163776, and *Gaia* 15458632-2638884992. All of these stars have photometry in only one *Gaia* band. The first two objects lack measurements of proper motion and parallax. Those parameters have large uncertainties for *Gaia* 148400225409163776 but are similar to the measurements for its primary. The proper motions and parallaxes of *Gaia*

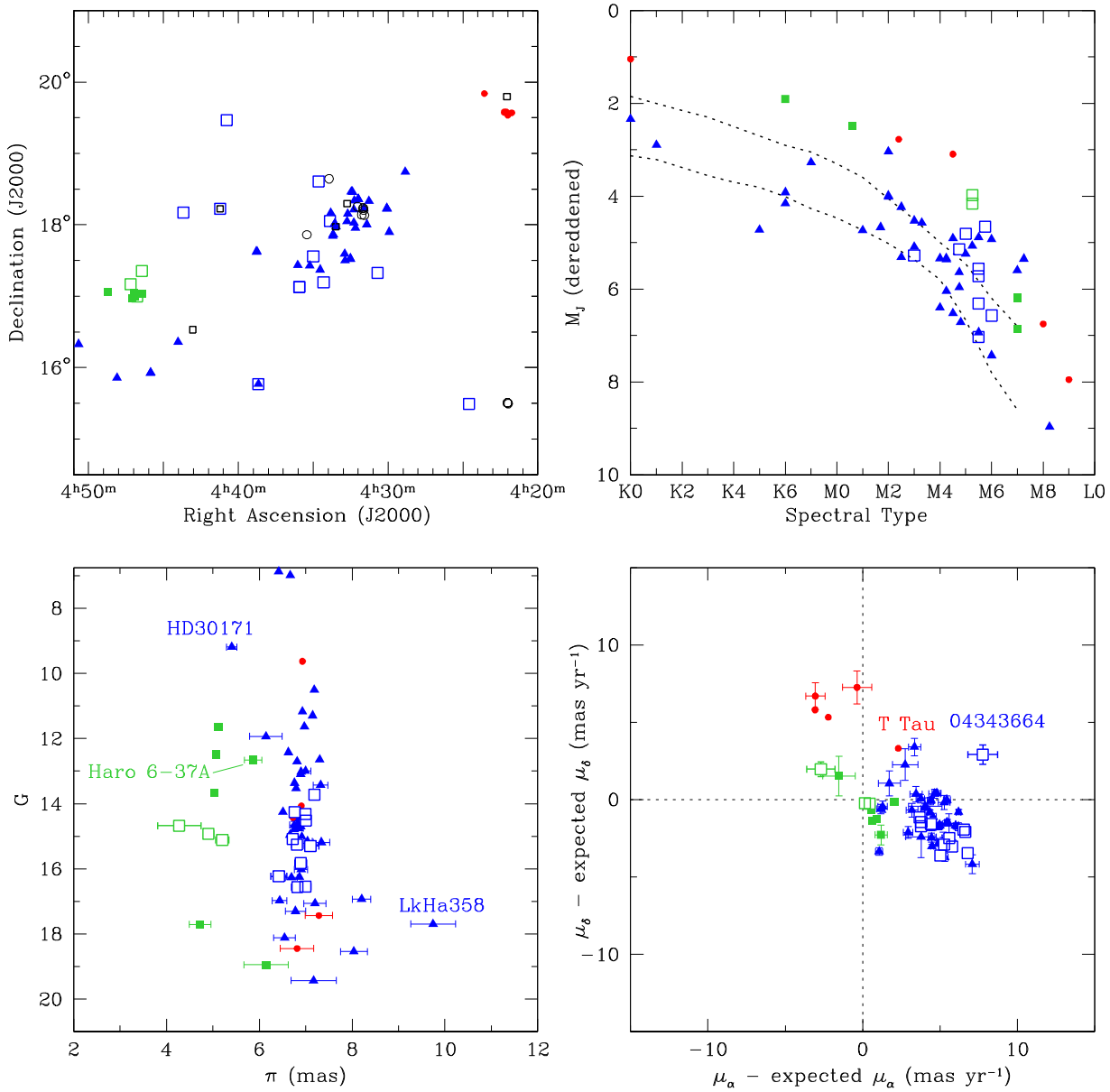

Figure 8. Same as Figure 2, but for members projected against the L1551 and L1558 clouds and a small cloud near T Tau.

154586322638884992 and its primary differ significantly, but the latter may have unreliable astrometry based on the large value of its RUWE (7.2).

The six candidates discussed in this section that lack spectroscopy are listed in Table 2.

5. Spectroscopy of Candidate Members

5.1. Observations

We have obtained spectra of 140 candidate members of Taurus identified in Sections 3 and 4,[5] three known companions that lack spectral classifications, and the primary for one of the latter stars. We also searched for publicly available spectra of our candidates in the data archives of observatories and spectroscopic surveys, finding spectra with sufficient signal-to-noise ratios (S/Ns) for 38 objects. Those archival observations consist of 31 optical spectra from the third data release of the Large Sky Area Multi-Object Fiber Spectroscopic Telescope survey (LAMOST; Cui et al. 2012; Zhao et al. 2012) and seven IR spectra collected through programs GN-2017A-Q-81, GN-2017B-Q-35 (L. Albert), and GN-2017B-Q-19 (E. Magnier) with the Gemini Near-Infrared Spectrograph (GNIRS; Elias et al. 2006). We present spectra for a total of 168 objects, some of which were observed with multiple instruments. This spectroscopic sample includes 61 of the 62 candidates identified by Luhman (2018), three additional stars from that study that did not satisfy the criteria for candidacy but were located very close to candidates (see Section 4), three known companions in Taurus that lack measured spectral types (JH223 B, XEST 20-071 B, V892 Tau NE), and XEST 20-071 A, which was observed at the same time as its companion. The remaining 100 targets in our sample were selected from the candidates identified in Section 3. The highest priority was given to candidates within the area of full *JHK* coverage from WFCAM (Figure 11).

[5] Three of these candidates were found independently by Zhang et al. (2018) and are treated as previously known members in this work.

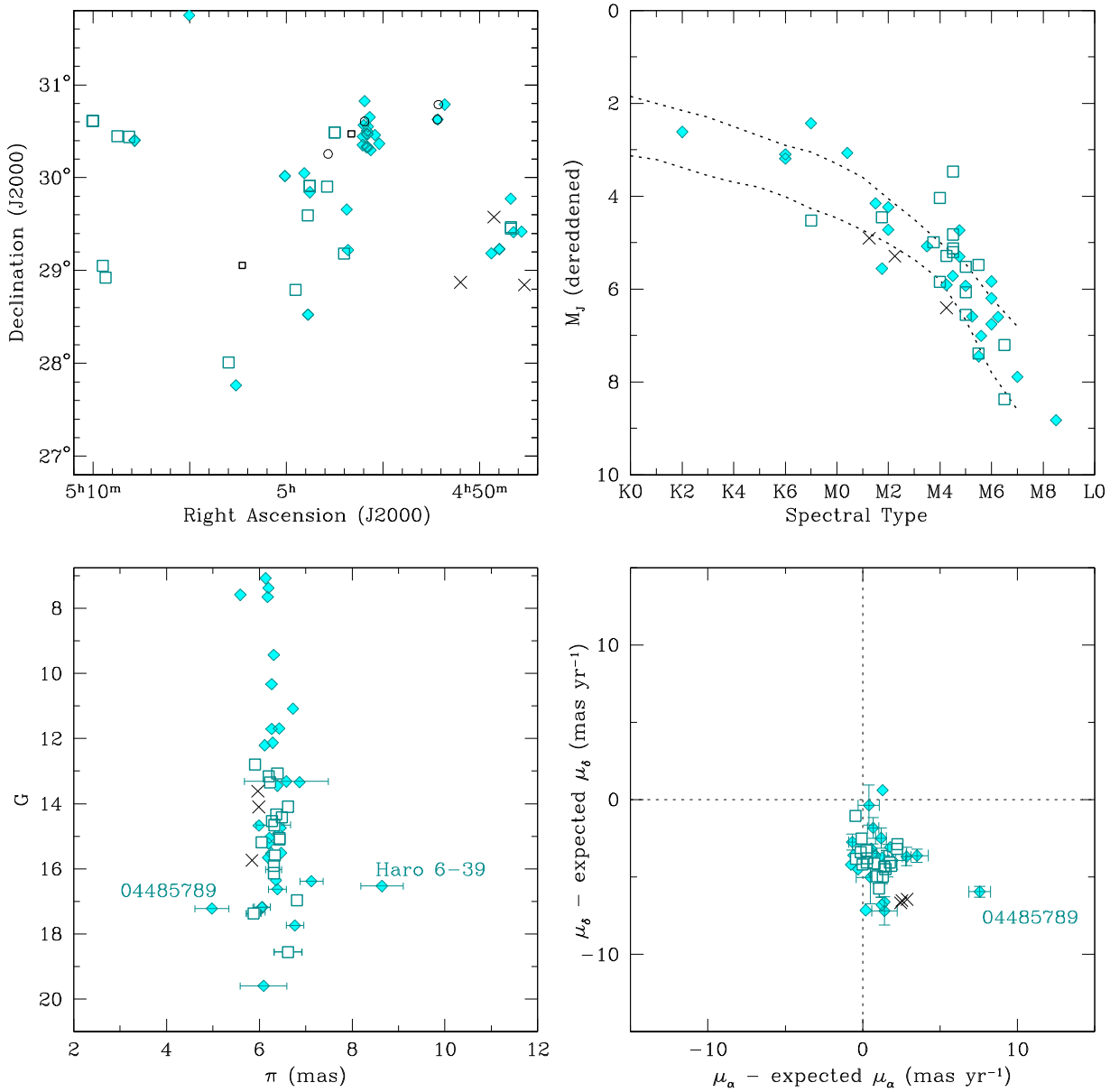

Figure 9. Same as Figure 2, but for members projected against the L1517 cloud. 2MASS J04474012+2850409, 2MASS J04491437+2934354, and 2MASS J04505864+2852218 (crosses) share very similar parallaxes, proper motion offsets, and ages, indicating that they are likely associated with each other. Their kinematics are distinct from those of the population of Taurus members within this field, so they are treated as nonmembers.

Table 2
Remaining Candidate Members of Taurus from *Gaia*

Gaia DR2 Source Name	α (J2000)[a] (deg)	δ (J2000)[a] (deg)	G[a]	RUWE[b]	Notes
152416436441091584	65.288914	27.843579	16.487	2.25	0.″76 from M5.25 member *Gaia* 152416436443721728
148400225409163776	69.936483	26.031919	20.392	1.50	3.″11 from M5 member ITG 15
154586322638884992	71.227352	27.296130	12.325	1.34	1.″81 from K1 member HD 283782
157816855305858176	71.458678	28.660584	6.724	2.37	HD 30111
157816859599833472	71.460272	28.659692	12.123	1.17	5.″97 from candidate HD 30111
3415706130945884416	78.115078	22.897051	14.303	9.74	0.″64 from M2.5 member *Gaia* 3415706130944329216

Notes.
[a] *Gaia* DR2.
[b] Lindegren (2018).

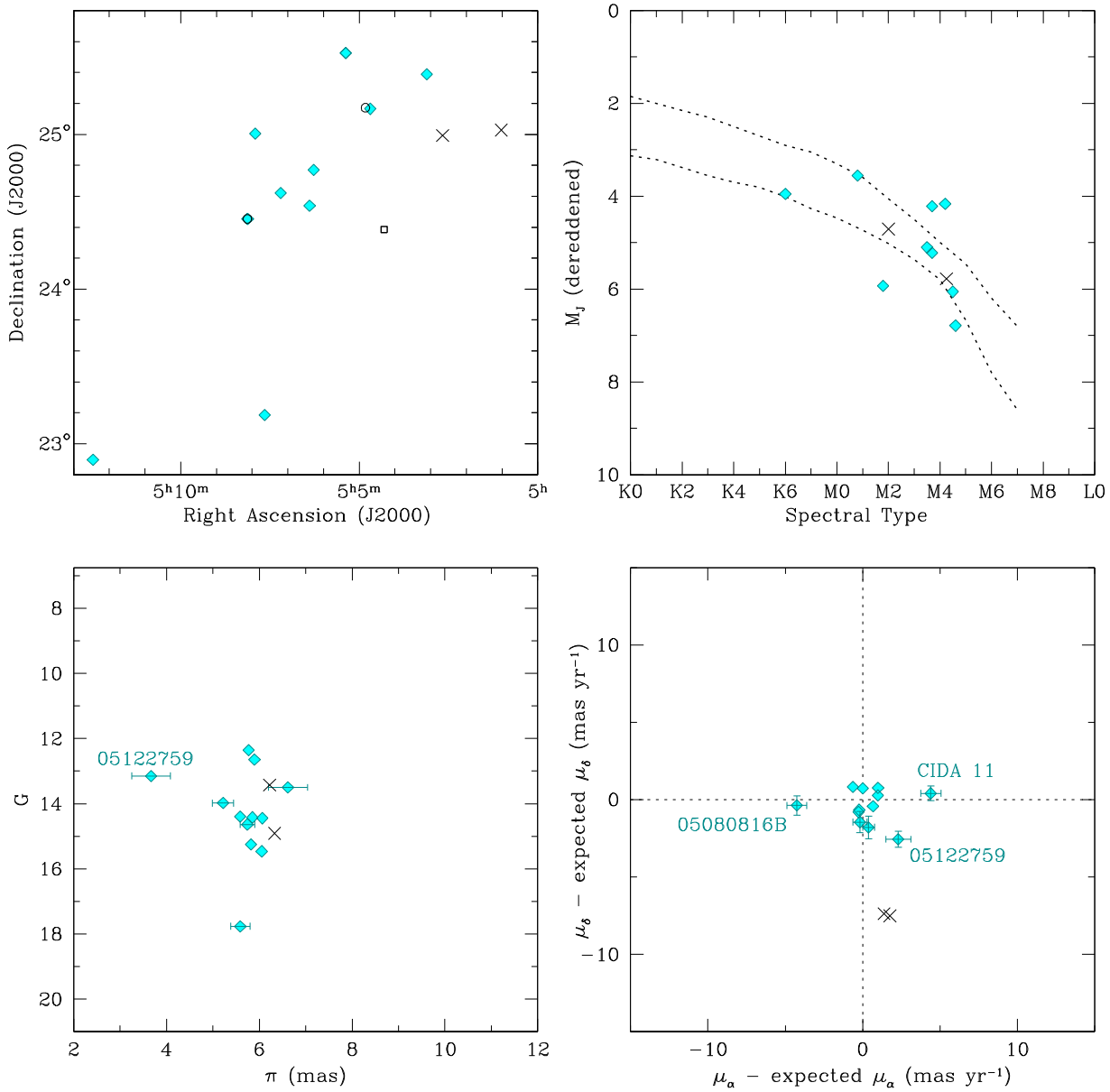

Figure 10. Same as Figure 2, but for members projected against the L1544 cloud. 2MASS J05010116+2501413 and 2MASS J05023985+2459337 (crosses) share very similar parallaxes, proper motion offsets, and ages, indicating that they are likely associated with each other. Their kinematics are distinct from those of the population of Taurus members within this field, so they are treated as nonmembers.

Table 3
Observing Log

Telescope/Instrument	Disperser/Aperture	Wavelengths/Resolution	Targets
HET/LRS2	VPH grisms/0.″6 lenslets	0.65–1.05 μm/1800	2
IRTF/SpeX	prism/0.″8 slit	0.8–2.5 μm/150	41
Gemini North/GMOS	R400/0.″5 slit	0.6–1.0 μm/2000	21
Gemini North/GNIRS	31.7 l mm^{-1}/1″ slit	0.9–2.5 μm/600	51
LAMOST	540 l mm^{-1}/3.″3 fiber	0.37–0.9 μm/1500	31
MMT/Red Channel	270 l mm^{-1}/0.″75 slit	0.58–0.92 μm/1000	34
MMT/Red Channel	1200 l mm^{-1}/0.″75 slit	0.63–0.71 μm/3250	18
MMT/MMIRS	HK grism/1.″2 slit	1.25–2.34 μm/600	8

We performed our spectroscopy with the Red Channel Spectrograph (Schmidt et al. 1989) and the MMT and Magellan Infrared Spectrograph (MMIRS; McLeod et al. 2012) at the MMT; GNIRS and the Gemini Multi-Object Spectrograph (GMOS; Hook et al. 2004) at Gemini North; SpeX (Rayner et al. 2003) at the NASA Infrared Telescope Facility (IRTF); and the Low-Resolution

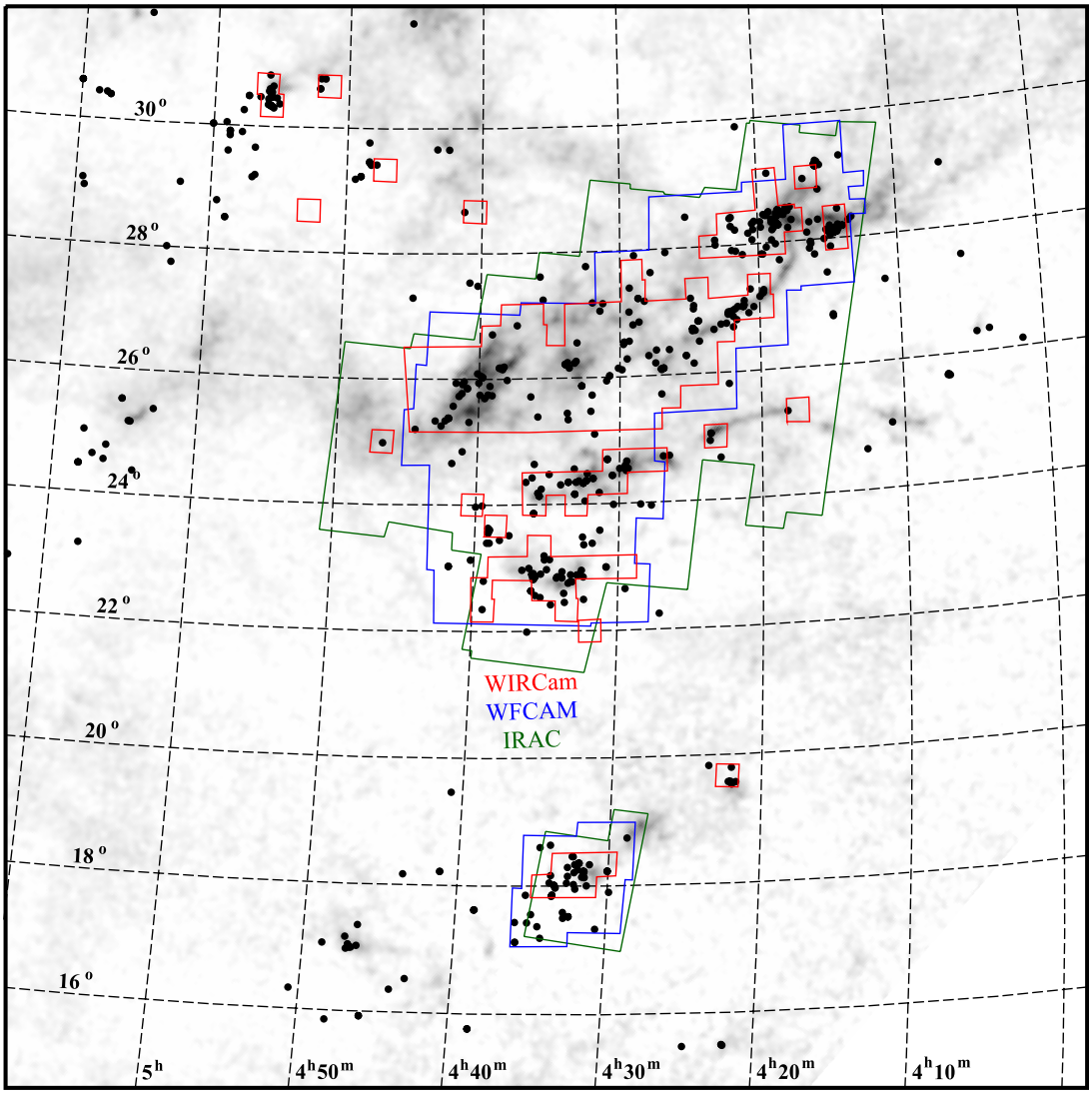

Figure 11. Fields in Taurus that have been imaged with IRAC, WIRCam, and in *JHK* with WFCAM (UKIDSS, UHS, new data). The dark clouds are displayed with a map of extinction (gray scale; Dobashi et al. 2005).

Table 4
Spectroscopic Data for Candidate Members of Taurus

Source Name[a]	Spectral Type	W_{λ}(Li) (Å)	Instrument	Date	Member?[c]
2MASS J04002788+2031591	M6.5	···	GNIRS	2017 Sep 2	N
2MASS J04005482+2117211	M8	···	GNIRS	2017 Sep 27	N
2MASS J04005866+2014043	M4	<0.2	SpeX, Red(1200)	2017 Oct 28, 2018 Jan 2	N
UGCS J040132.09+260733.2	M9.5,M9.5	···	SpeX, GNIRS	2017 Oct 30, 2017 Sep 29	Y
2MASS J04053214+2733139	M4.75	···	Red(270)	2017 Oct 22	N?

Note.
[a] Identifications from the 2MASS Point Source Catalog when available. Otherwise, they are based on coordinates from data release 10 of the UKIDSS Galactic Clusters Survey.

(This table is available in its entirety in machine-readable form.)

Spectrograph 2 (LRS2; Chonis et al. 2014, 2016) at the Hobby-Eberly Telescope (HET). The instrument configurations are summarized in Table 3. The date and instrument for each object are listed in Table 4. The archival data from LAMOST and GNIRS have been included in Tables 3 and 4.

We reduced the data from SpeX with the Spextool package (Cushing et al. 2004) and corrected them for telluric absorption using spectra of A0V stars (Vacca et al. 2003). The GNIRS and MMIRS data were reduced and corrected for telluric absorption in a similar manner using routines within IRAF. The optical

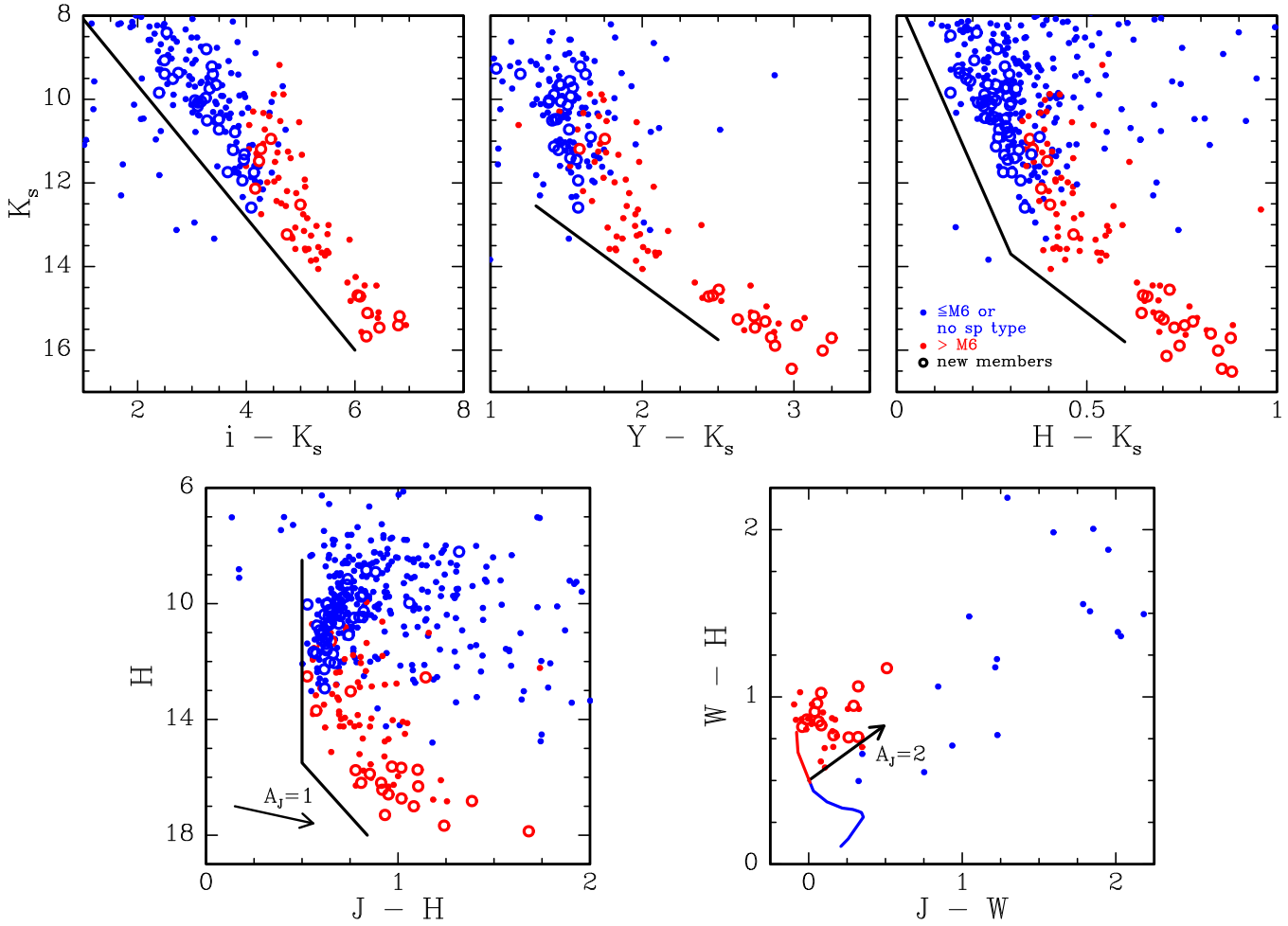

Figure 12. Selection of CMDs and a color–color diagram for previously known members of Taurus (filled circles) and new members from this work (open circles) based on photometry from *Gaia* DR2, 2MASS, WFCAM (UKIDSS, UHS, new data), and WIRCam. From the other stars detected in these surveys, we have selected candidate members based on positions above the solid boundaries in the CMDs. The diagram of $W - H$ vs. $J - W$ includes the locus of young ⩽M6 and >M6 photospheres (blue and red lines) and is used only for identifying possible late-type members based on colors above the reddening vector. The data in the top row of diagrams have been corrected for extinction.

spectra from Red Channel and GMOS were also reduced with IRAF. The LRS2 data were processed with the LRS2 Quick-Look Pipeline (B. L. Indahl 2019, in preparation), which is briefly described by Davis et al. (2018). Fully reduced spectra are provided by the LAMOST survey. We present examples of the reduced optical and IR spectra in Figures 15 and 16, respectively. All of the reduced spectra are provided in electronic files that accompany those figures with the exception of the LAMOST data, which are available from http://www.lamost.org.

5.2. Spectral Classification

We have used the spectra from the previous section to estimate spectral types and to identify evidence of youth that would support membership in Taurus. Given their colors and magnitudes, the candidates in our spectroscopic sample should have M/L spectral types if they are members. For these types, we have utilized diagnostics of youth that include Li I absorption at 6707 Å and gravity-sensitive features like the Na I doublet near 8190 Å and the shape of the *H*-band continuum (Martín et al. 1996; Luhman et al. 1997; Lucas et al. 2001). Our measurements of the equivalent widths of Li I are listed in Table 4 and are plotted versus spectral type in Figure 17. For the range of spectral types of the objects with useful Li constraints (⩾K7), most known members of Taurus have equivalent widths of $\gtrsim$0.4 Å (Basri et al. 1991; Magazzú et al. 1992; Martín et al. 1994). For young objects at <M5 and field dwarfs, we classified the optical spectra through comparison to dwarf standards (Kirkpatrick et al. 1991, 1997; Henry et al. 1994). The optical data for young sources at ⩾M5 were classified with the average spectra of dwarf and giant standards (Luhman et al. 1997; Luhman 1999a). For the near-IR spectra, we applied young standards (Luhman et al. 2017) and dwarf standards (Cushing et al. 2005; Rayner et al. 2009) as appropriate. The resulting classifications are listed in Table 4. For the young objects that were observed with IR spectroscopy, we have used the slopes of those data relative to the best-fitting standards to derive estimates of extinction. Spectra of young L dwarfs with low-to-moderate S/Ns can be matched by standards across a wide range of types when extinction is a free parameter (Luhman et al. 2017), as illustrated in Figure 16, where three of the coolest new members are compared to standard spectra bracketing their classifications.

Moderately young stars (∼10–100 Myr) that are unrelated to the Taurus clouds (∼2 Myr; Palla & Stahler 2000) are scattered

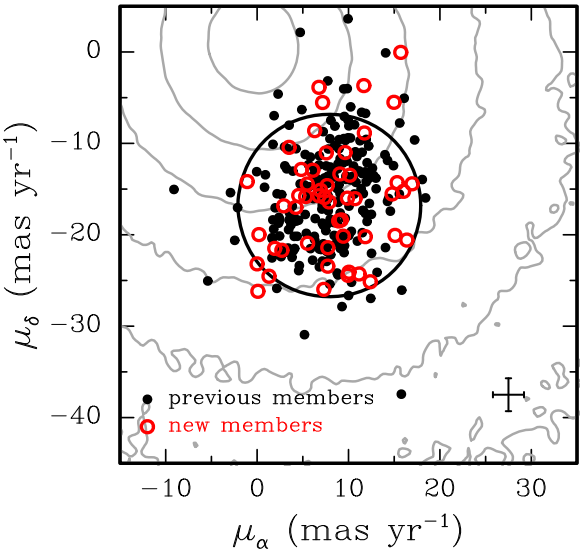

Figure 13. Relative proper motions for known members of Taurus (filled circles) and new members from this work (open circles) based on astrometry from 2MASS, WFCAM (UKIDSS, UHS, new data), and IRAC. Measurements for other sources projected against Taurus are represented by contours at log (numbers/(mas yr^{-1})^2) = 1, 1.5, 2, 2.5, 3, and 3.5. Sources within 1σ of the large circle are selected as candidate members. The typical errors for these data are indicated.

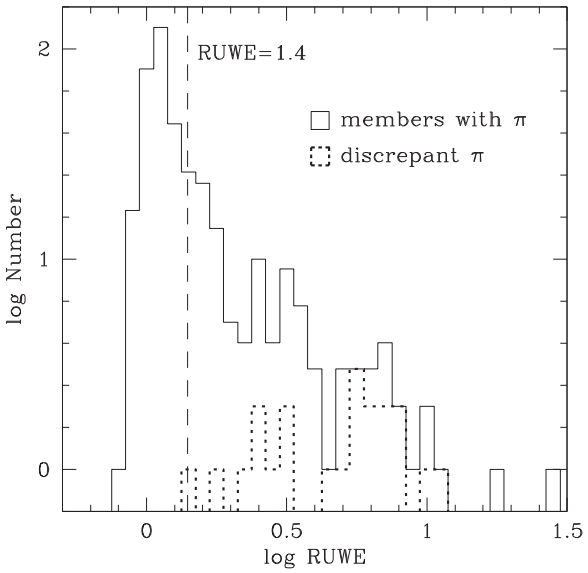

Figure 14. Distributions of log(RUWE) for known members of Taurus with parallax measurements from *Gaia* DR2 (solid histogram) and the members with discrepant parallaxes (dotted histogram, Luhman 2018, Appendix). Lindegren (2018) suggested that RUWE $\lesssim$ 1.4 indicates a good astrometric fit and reliable astrometry (dashed line).

across the large field that we have selected for our survey (Luhman 2018, references therein). As a result, a spectroscopic signature of youth may not be sufficient evidence of membership in Taurus, particularly if it provides only a rough constraint on age (e.g., <100 Myr). In addition, some of the young contaminants have proper motions that are close enough to those of Taurus members that the former can appear to have

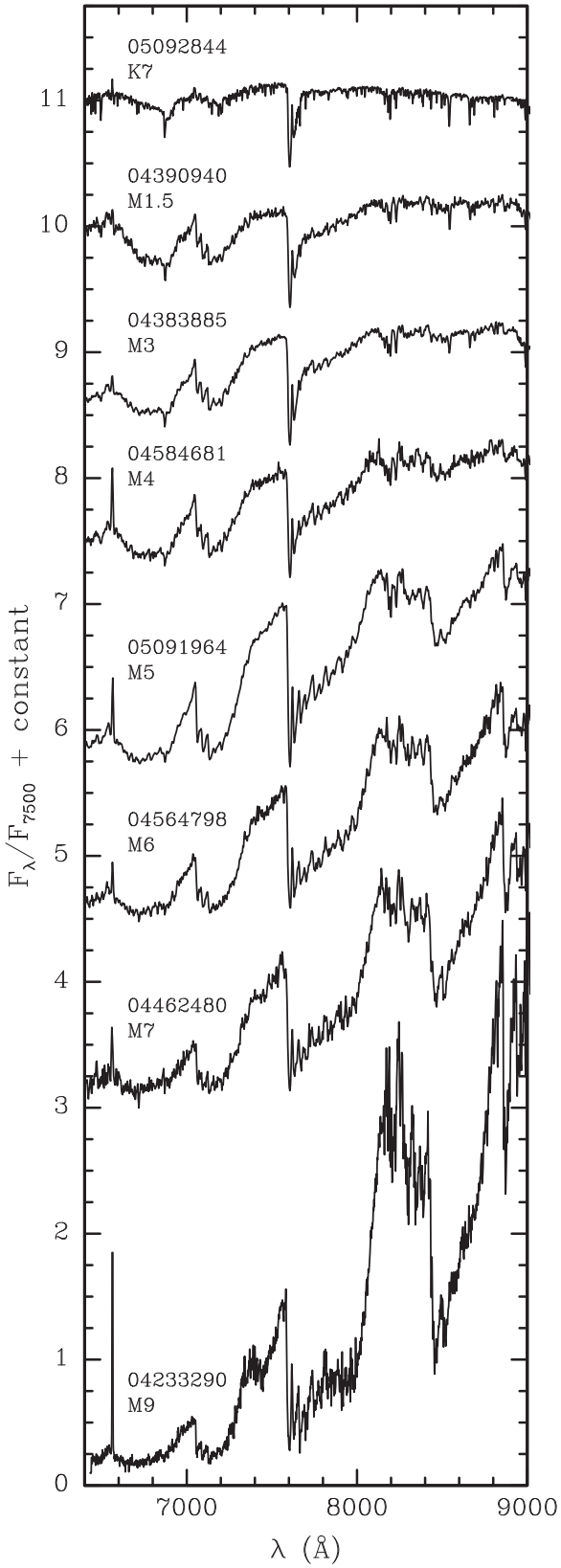

Figure 15. Examples of optical spectra of new Taurus members (Table 4). These data are displayed at a resolution of 13 Å. The data used to create this figure are available.

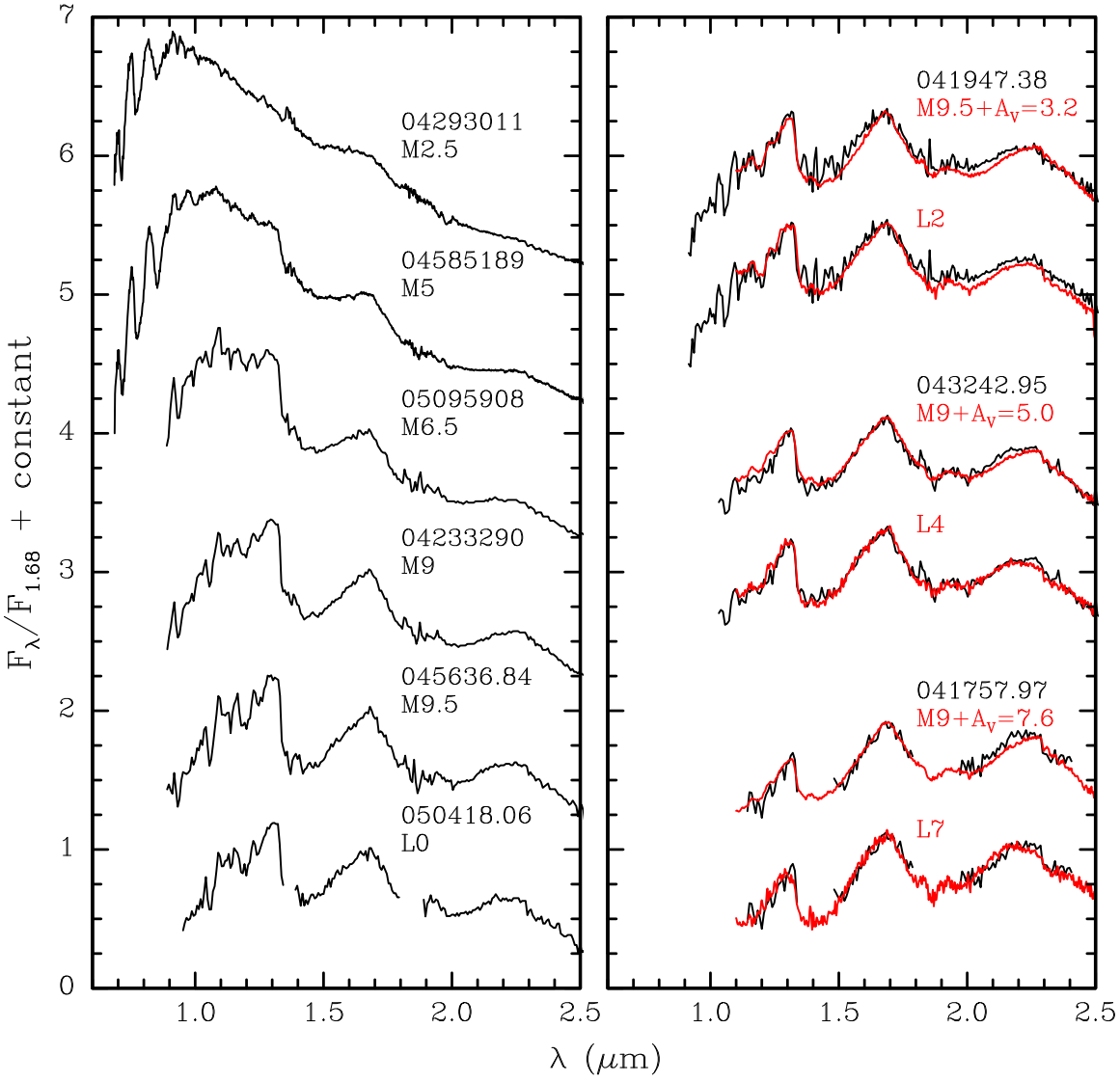

Figure 16. Examples of IR spectra of new Taurus members (Table 4). The spectra in the left panel have been dereddened to match the slopes of the young standards from Luhman et al. (2017). In the right panel, the observed spectra of three of the coolest objects are compared to standard spectra that bracket their classifications. The data used to create this figure are available.

motions consistent with membership when the errors are $\gtrsim$3 mas yr^{-1}, which applies to most non-*Gaia* data (Luhman 2018). Given these considerations, we have taken the following approach to assigning membership in our spectroscopic sample. We treat an object as a member if its proper motion and parallax from *Gaia* DR2 support membership (i.e., the candidates from Luhman 2018) and its spectrum shows evidence of youth, which is taken to be $W_\lambda \gtrsim 0.4$ Å when a Li measurement is available. If Li is detected at a weaker level ($\gtrsim$0.15 Å) and the *Gaia* data agree closely with those of known members, we also adopt the star as a member (Appendix). Candidate companions to known members are adopted as members if they have spectroscopic signatures of youth. Discrepant *Gaia* astrometry is ignored when the astrometric fit is poor (RUWE $\gtrsim$ 1.4), which applies to some of the candidate companions. If *Gaia* does not offer reliable measurements of parallax and proper motion, a candidate is adopted as a member if its available proper motion data are consistent with membership, its spectrum shows evidence of youth, it appears within the sequence of known members in CMDs and in a diagram of M_K versus spectral type, and it is within $\sim$1° of known members.

Based on the above criteria, 86 of the 168 objects in our spectroscopic sample are members of Taurus, as indicated in Table 4. Three members were previously known companions that lacked spectral classifications, one member is the primary for one of those companions, and three members were independently found in a recent survey (Zhang et al. 2018). The remaining 79 members are newly confirmed in this work. As discussed in Section 2, the census of Taurus now contains 519 known members. Our survey has doubled the number of known members at $\geqslant$M9 and has uncovered the faintest known members in M_K, as illustrated in Figure 18, where we show extinction-corrected M_K versus spectral type for previously known members and our new members. UGCS J041757.97 +283233.9 is now the faintest known member. It has a very red spectrum, which is consistent with spectral types ranging from M9 ($A_V = 7.6$) to L7 ($A_V = 0$), as illustrated in Figure 16.

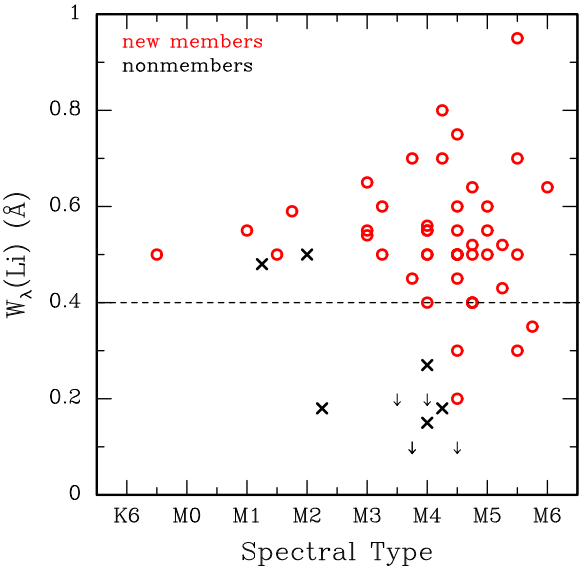

Figure 17. Equivalent widths of Li vs. spectral type for candidate members of Taurus. Known members of Taurus at these types typically have equivalent widths of $\gtrsim$0.4 Å (dashed line; Basri et al. 1991; Magazzú et al. 1992; Martín et al. 1994). The candidates have been classified as members (circles) or nonmembers (crosses) based on a combination of their Li strengths and their *Gaia* astrometry (see Section 5.2 and the Appendix).

Assuming a *K*-band bolometric correction for young L dwarfs (Filippazzo et al. 2015), the median parallax of 7.8 mas for the nearest group of members, and $A_V = 3.5$, we estimate $\log L_{\rm bol} = -3.76$ for UGCS J041757.97+283233.9, which implies a mass of 0.003–0.01 $M_\odot$ (~3–10 $M_{\rm Jup}$) for ages of 1–10 Myr according to evolutionary models (Burrows et al. 1997; Chabrier et al. 2000).

Most (54/61) of the candidate members identified with *Gaia* data by Luhman (2018) have been adopted as Taurus members. Among the other candidates that were not part of that sample, 39 are field stars that were observed prior to our WFCAM imaging and the release of *Gaia* DR2 and that would be rejected by our current criteria that incorporate those data.

Luhman (2018) found that members of Taurus exhibit four distinct populations in terms of parallax and proper motion, which were given names of red, blue, green, and cyan. We have assigned the new members to those populations when the necessary data are available from *Gaia* DR2, as indicated in Table 1 and Figures 2–10.

Comments on the spectral types, membership, and kinematics of individual objects are provided in the Appendix.

6. Circumstellar Disks

6.1. Disk Detection and Classification

We have compiled the available mid-IR photometry of the new members of Taurus from this work to check for evidence of circumstellar disks via the presence of IR emission in excess above the expected photospheric emission. We also have performed this analysis on members adopted by Luhman (2018) that were not examined for disks by Esplin & Luhman (2017) or earlier studies. We make use of photometry in *W*1–*W*4 from the AllWISE Source Catalog, [3.6]–[8.0] from IRAC on *Spitzer*, and the 24 μm band of the Multiband Imaging Photometer for *Spitzer* (MIPS; Rieke et al. 2004), which is denoted as [24]. The *Spitzer* data were measured in the manner described by Luhman et al. (2010). We present the resulting *WISE* and *Spitzer* data in Table 1. In addition, we have included photometry from those facilities for previously known members (Luhman et al. 2010; Esplin et al. 2014; Esplin & Luhman 2017).

To determine whether excess mid-IR emission is present in a given object and to classify the evolutionary stage of a detected disk, we have followed the methods and terminology described in Luhman et al. (2010) and Esplin et al. (2014) (see also Esplin et al. 2018). In summary, we calculated extinction-corrected colors of the mid-IR photometry relative to K_s, measured color excesses relative to photospheric colors, and used the sizes of those excesses (when present) to estimate the evolutionary stages of the disks. The colors utilized for that analysis are plotted as a function of spectral type in Figure 19 for both previously known members and the newly classified members. The disks are assigned to the following categories: optically thick *full* (primordial) disks with no large gaps or holes that affect the mid-IR spectral energy distribution (SED), optically thick *transitional* disks with large inner holes, optically thin *evolved* disks with no large gaps, optically thin *evolved transitional* disks with large inner holes, and optically thin *debris* disks that are composed of second-generational dust from planetesimal collisions (Kenyon & Bromley 2005; Rieke et al. 2005; Hernández et al. 2007; Luhman et al. 2010; Espaillat et al. 2012).

The Taurus members that have been found since Esplin & Luhman (2017) are plotted with red and blue symbols in Figure 19 according to the presence or absence of excess emission, respectively. Ten of those stars exhibit mid-IR excess emission. Four of them have excesses only in [24] or *W*4, although one of them, HD 30378 (B9.5), is only slightly below our adopted excess threshold in *W*3. The excesses are small (~0.5 mag) for the other three stars with excesses in only [24]/*W*4, which consist of 2MASS J04355694+2351472 (M5.75), 2MASS J04390571+2338112 (M6), and 2MASS J04584681+2954407 (M4). Two M9.5 members, 2MASS J04213847+2754146 and UGCS J042438.53+264118.5, have excesses in [4.5], *W*2, and [8.0] and lack reliable detections at longer wavelengths. 2MASS J04451654+3141202 (M5.5) has excesses in *W*2 and *W*3. It is blended with another source in the *WISE* images, but it clearly dominates in *W*3. 2MASS 04282999+2358482 (M9.25) and UGCS J043907.76+264236.0 (M9.5–L4) have marginal excesses at [8.0], and UGCS J041757.97+283233.9 (M9-L7) has a marginal excess at [4.5]. The latter is the faintest known member in extinction-corrected *K*. It is difficult to reliably identify the presence of excess emission for the coolest members because of the uncertainties in the photospheric colors and the spectral classifications of young L-type objects (Esplin & Luhman 2017; Esplin et al. 2017). The evolutionary stages assigned to the newly identified disks are presented in Table 1, where we also include the classifications of previously known members (Luhman et al. 2010; Esplin et al. 2014; Esplin & Luhman 2017).

6.2. Disk Fraction

Luhman et al. (2010) measured the fraction of Taurus members that have disks as a function of spectral type (and hence mass) for known members observed by *Spitzer*. Since that study, mid-IR photometry has become available for additional members from both *Spitzer* and *WISE*, and many

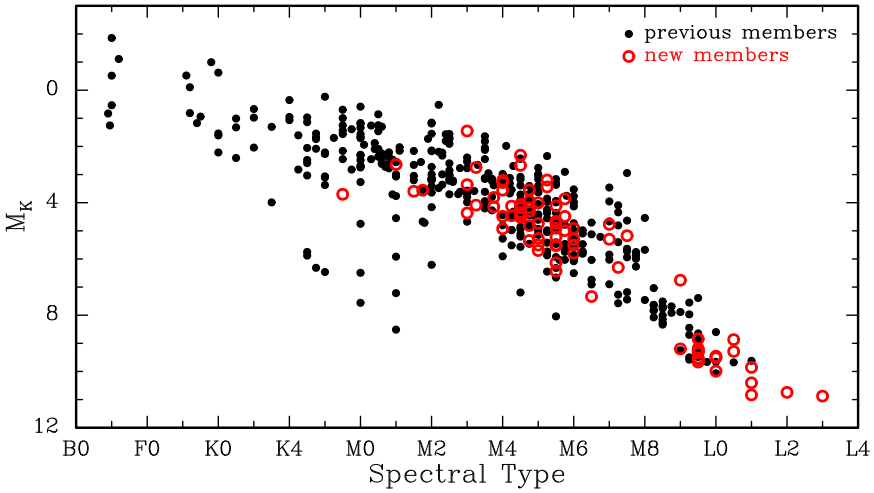

Figure 18. Extinction-corrected M_K vs. spectral type for the previously known members of Taurus (filled circles) and new members from this work (open circles). The stars that are below the sequence may be seen primarily in scattered light, which is plausible given that they have evidence of circumstellar disks. If a parallax measurement is unavailable for a given member, we have derived M_K using the median parallax for the closest Taurus population.

new members have been identified. Therefore, it would be worthwhile to perform a new calculation of the disk fraction in Taurus using our new catalog of members.

The evolutionary stages of young stellar objects consist of Classes 0 and I (protostar+disk+infalling envelope), Class II (star+disk), and Class III (star without disk; Lada & Wilking 1984; Lada 1987; André et al. 1993; Greene et al. 1994). Taurus members that have been previously designated as Class 0 or Class I are marked as such in Table 1. We consider all other members with disks to be Class II objects. Some disks have classifications of "debris/evolved transitional" because we cannot distinguish between these two classes with the available data. Stars with debris disks are normally counted as Class III objects, but since very few debris disks are expected in a region as young as Taurus, we treat all of the "debris/evolved transitional" disks as Class II.

As done in Luhman et al. (2010), we define the disk fraction as $N(\mathrm{II})/N(\mathrm{II+III})$ and measure it as a function of spectral type using bins of <K6, K6–M3.5, M3.75–M5.75, M6–M8, and M8–M9.75. We exclude stars that lack measured spectral types, all of which are protostars or close companions. We also omit objects with spectral types of $\geqslant$L0 because of the difficulty in reliably identifying the presence of excess emission from disks (Section 6.1). The resulting disk fraction is tabulated and plotted in Table 5 and Figure 20, respectively.

The current census of Class II members of Taurus should have a high level of completeness for spectral types earlier than ~M8 (Esplin et al. 2014). However, the census may be incomplete for Class III at high extinctions, which would lead to an overestimate of the disk fraction when all known members are considered. To investigate this possibility, we have computed disk fractions for samples of members that should be complete for both Classes II and III. Now that most of the candidate members identified with *Gaia* by Luhman (2018) have been observed spectroscopically, the census should be complete for both Class II and Class III members earlier than M6–M7 at low extinctions ($A_J < 1$; Luhman 2018). Meanwhile, the census within the WFCAM field in Figure 11 should be complete for $\lesssim$L0 at $A_J < 1.5$ (Section 7.1). We find that the disk fractions for $A_J < 1$ across the entirety of Taurus and for $A_J < 1.5$ within the WFCAM fields are indistinguishable from the disk fraction in Figure 20 for all known members.

Table 5
Disk Fraction for Taurus

Spectral Type	$N(\mathrm{II})/N(\mathrm{II+III})$
<K6	$24/33 = 0.73^{+0.06}_{-0.09}$
K6–M3.5	$102/143 = 0.71^{+0.03}_{-0.04}$
M3.75–M5.75	$64/148 = 0.43 \pm 0.04$
M6–M8	$21/63 = 0.33^{+0.06}_{-0.05}$
>M8–M9.75	$15/37 = 0.41^{+0.08}_{-0.07}$

The disk fraction in Figure 20 is near ~0.7 and 0.4 for spectral types of $\leqslant$M3.5 and >M3.5, respectively. A similar trend with spectral type was present in the data from Luhman et al. (2010), although the disk fraction was slightly higher than our new measurement (~0.75 and 0.45). The disk fraction in Taurus is similar to that in Chamaeleon I, which is ~0.7 and 0.45 for $\leqslant$M3.5 and >M3.5, respectively (Luhman et al. 2010). For all spectral types combined, Taurus has a disk fraction of ~0.5, which is roughly similar to the disk fractions of IC 348 and NGC 1333 (~0.4 and 0.6). However, those two clusters do not show a variation with spectral type (Luhman et al. 2016).

7. Initial Mass Function

7.1. Completeness

To derive constraints on the IMF in Taurus from our new census of members, we begin by evaluating the completeness of that census.

In Section 3, we focused on the identification of candidate substellar members within the WFCAM fields in Figure 11. To evaluate the completeness of our census within that field, we employ a CMD constructed from H and K_s, which offer the greatest sensitivity to low-mass members of Taurus among the available bands. In Figure 21, we plot K_s versus $H - K_s$ for the known members in the WFCAM fields and all other sources in those fields that (1) are not rejected by the photometric and proper motion criteria from Section 3 or the astrometric criteria from Luhman (2018) and (2) are not known nonmembers based on spectroscopy or other data. There are very few remaining sources with undetermined membership status within a wide range of

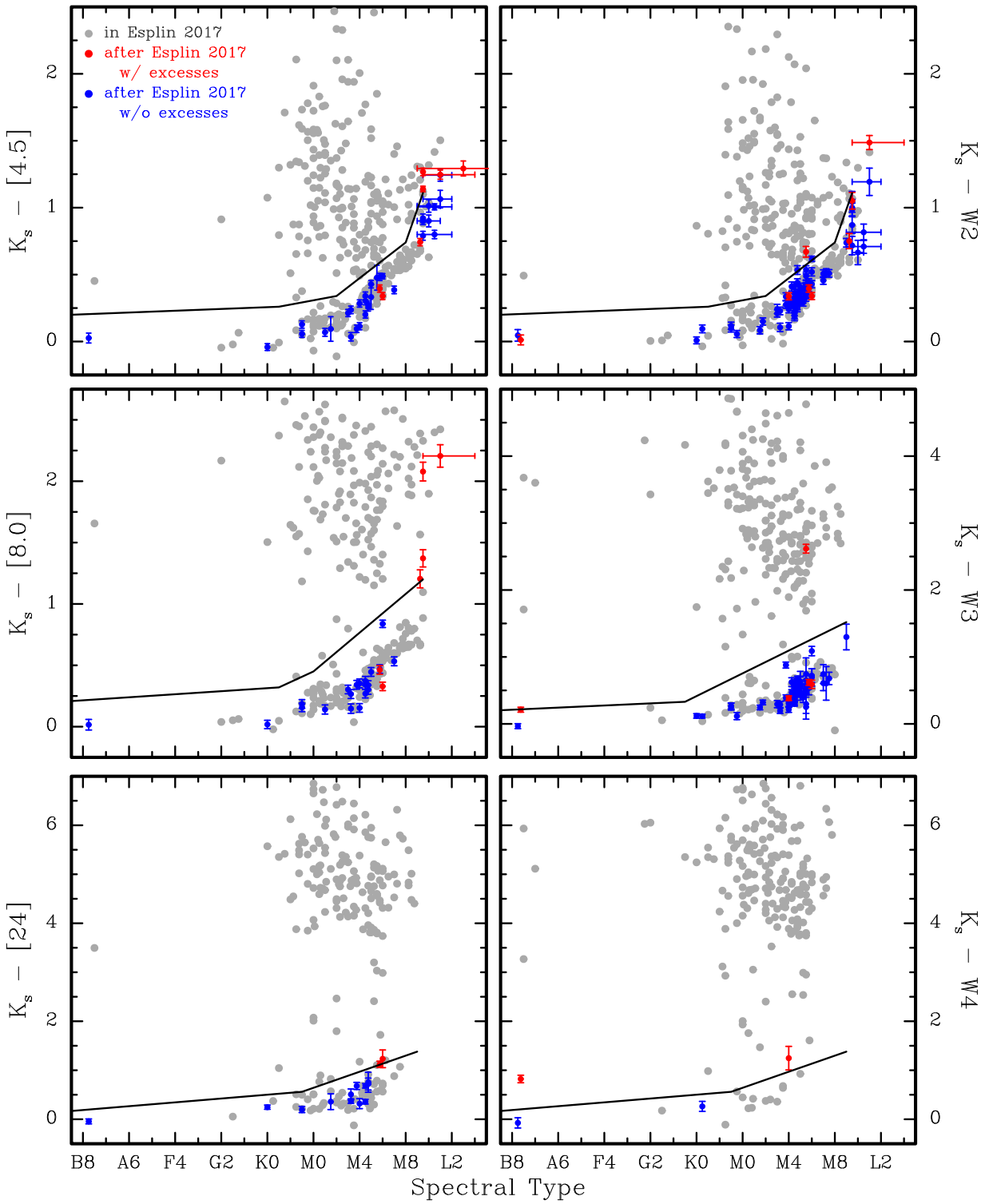

Figure 19. Extinction-corrected IR colors as a function of spectral type for known members of Taurus. The members that have been found since Esplin & Luhman (2017) are plotted with the errors in their colors and are represented by red and blue symbols according to presence or absence of excesses in these data. Excesses have been identified using the indicated thresholds (solid lines), which were selected to follow the observed photospheric sequence in each color (Esplin et al. 2014).

magnitudes and reddenings. For instance, the current census within the WFCAM fields should be complete for an extinction-corrected magnitude of $K_s < 15.7$ ($\lesssim$L0) for $A_J < 1.5$.

In Section 4, we adopted the candidate stellar members that were identified by Luhman (2018) using data for the entirety of Taurus from *Gaia* DR2. That study demonstrated that the census of Taurus should be complete for spectral types earlier than M6–M7 at $A_J < 1$ after including the *Gaia* candidates that are spectroscopically confirmed to be members.

7.2. Distributions of Spectral Type, M_K, and Mass

Based on the analysis in the previous section, we have defined two extinction-limited samples of known Taurus

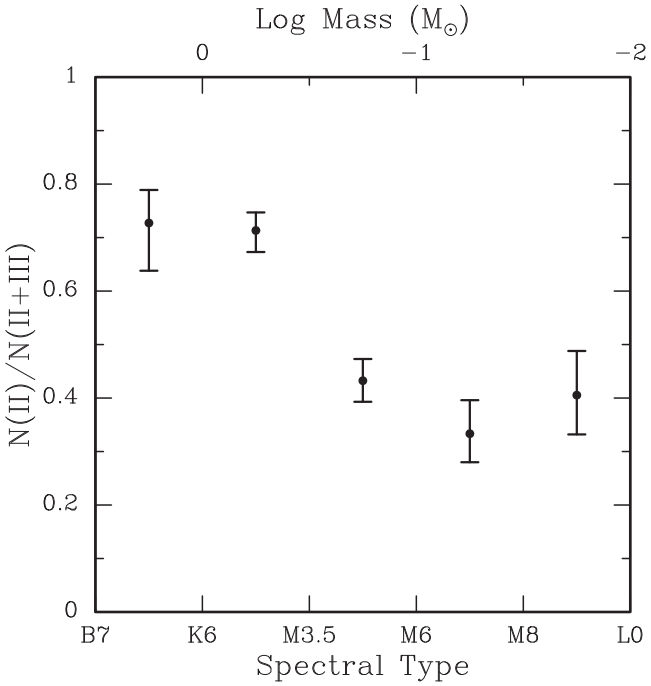

Figure 20. Fraction of Taurus members with circumstellar disks (Class II) as a function of spectral type (Table 5). The boundaries of the spectral type bins were chosen to correspond approximately to logarithmic intervals of mass.

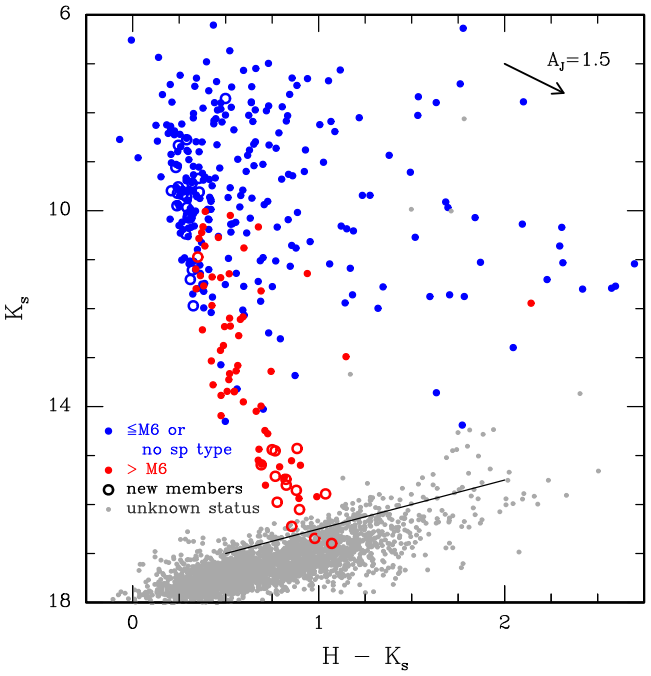

Figure 21. Near-IR CMD of the known members of Taurus within the WFCAM fields from Figure 11 (large filled and open circles) and the remaining sources in those fields with unconstrained membership (small gray points). The completeness limit of the photometry is indicated (solid line).

members that should have well-defined completeness limits, making them suitable for characterizing the IMF: members in the WFCAM fields with $A_J < 1.5$ and members at any location with $A_J < 1$. Stars that lack extinction estimates are excluded from these samples, which consist of protostars, close companions, and edge-on disks. As done in our recent studies of IC 348, NGC 1333, and Chamaeleon I (Luhman et al. 2016; Esplin et al. 2017), we use distributions of spectral types and extinction-corrected M_K as observational proxies for the IMF. The distributions of these parameters for our two extinction-limited samples are presented in Figure 22. For objects that lack parallax measurements, we derived M_K using the median parallax of the nearest population of members. In addition, we have estimated the IMF for each sample using distributions of spectral types in which the bins are selected to approximate logarithmic intervals of mass according to evolutionary models (Baraffe et al. 1998, 2015) and the temperature scale for young stars (Luhman et al. 2003), as done for the disk fraction in Figure 20. The resulting IMFs are shown in Figure 22.

The two samples of Taurus members in Figure 22 have similar distributions, which is not surprising given the large overlap between the fields in question (i.e., the WFCAM fields encompass a large majority of known members). Luhman (2018) found that an $A_J < 1$ sample of members with the *Gaia* candidates included exhibited a prominent maximum at M5 ($\sim$0.15 $M_\odot$) and thus resembled denser clusters like IC 348, NGC 1333, Chamaeleon I, and the Orion Nebula Cluster (Da Rio et al. 2012; Hillenbrand et al. 2013; Luhman et al. 2016; Esplin et al. 2017). Since we have confirmed most of the *Gaia* candidates as members, our $A_J < 1$ sample in Figure 22 has a similar distribution of spectral types as in Luhman (2018).

In the $A_J < 1.5$ sample for the WFCAM fields, the distributions of spectral type and M_K decrease rapidly below the peak and remain roughly flat at substellar masses down to the completeness limit, which corresponds to $\sim$5–13 $M_{\rm Jup}$ for ages of 1–10 Myr according to evolutionary models (Burrows et al. 1997; Chabrier et al. 2000). Thus, our completeness limit in that sample does not appear to be near a low-mass cutoff. The faintest known member, UGCS J041757.97+283233.9, has an estimated mass of $\sim$3–10 $M_{\rm Jup}$ (Section 5.2), which represents an upper limit on the minimum mass in Taurus. These results are consistent with recent surveys for brown dwarfs in other star-forming regions (Luhman et al. 2016; Esplin & Luhman 2017; Zapatero Osorio et al. 2017; Lodieu et al. 2018), young associations (Liu et al. 2013; Kellogg et al. 2015; Schneider et al. 2016; Best et al. 2017), and the solar neighborhood (Kirkpatrick et al. 2019), which have found that the IMF extends down to $\lesssim$5 $M_{\rm Jup}$. Using the minimum variance unbiased estimator for a power-law distribution, we calculate a slope of $\alpha = 1.0 \pm 0.1$[6] between the hydrogen-burning limit and the completeness limit (0.01–0.08 $M_\odot$) in the IMF for the $A_J < 1.5$ sample, which is shallower than the slope of $\alpha \sim -0.3$ in the lognormal mass function from Chabrie (2005).

8. Conclusion

In Esplin & Luhman (2017), we searched for substellar members of Taurus using photometry and proper motions from 2MASS, UKIDSS, PS1, SDSS, *Spitzer*, *WISE*, and *Gaia* DR1. We have identified additional candidate members by incorporating new data from UKIRT and CFHT. In Luhman (2018), candidate members at stellar masses were identified with high-precision proper motions and parallaxes from *Gaia* DR2. We have measured spectral types and assessed membership for candidates from these two samples using optical and IR spectra. Through this analysis, we have identified 79 new

[6] α is defined such that $dN/dM \propto M^{-\alpha}$. $\alpha = 1$ corresponds to a slope of zero when the mass function is plotted in logarithmic units, as done in Figure 22.

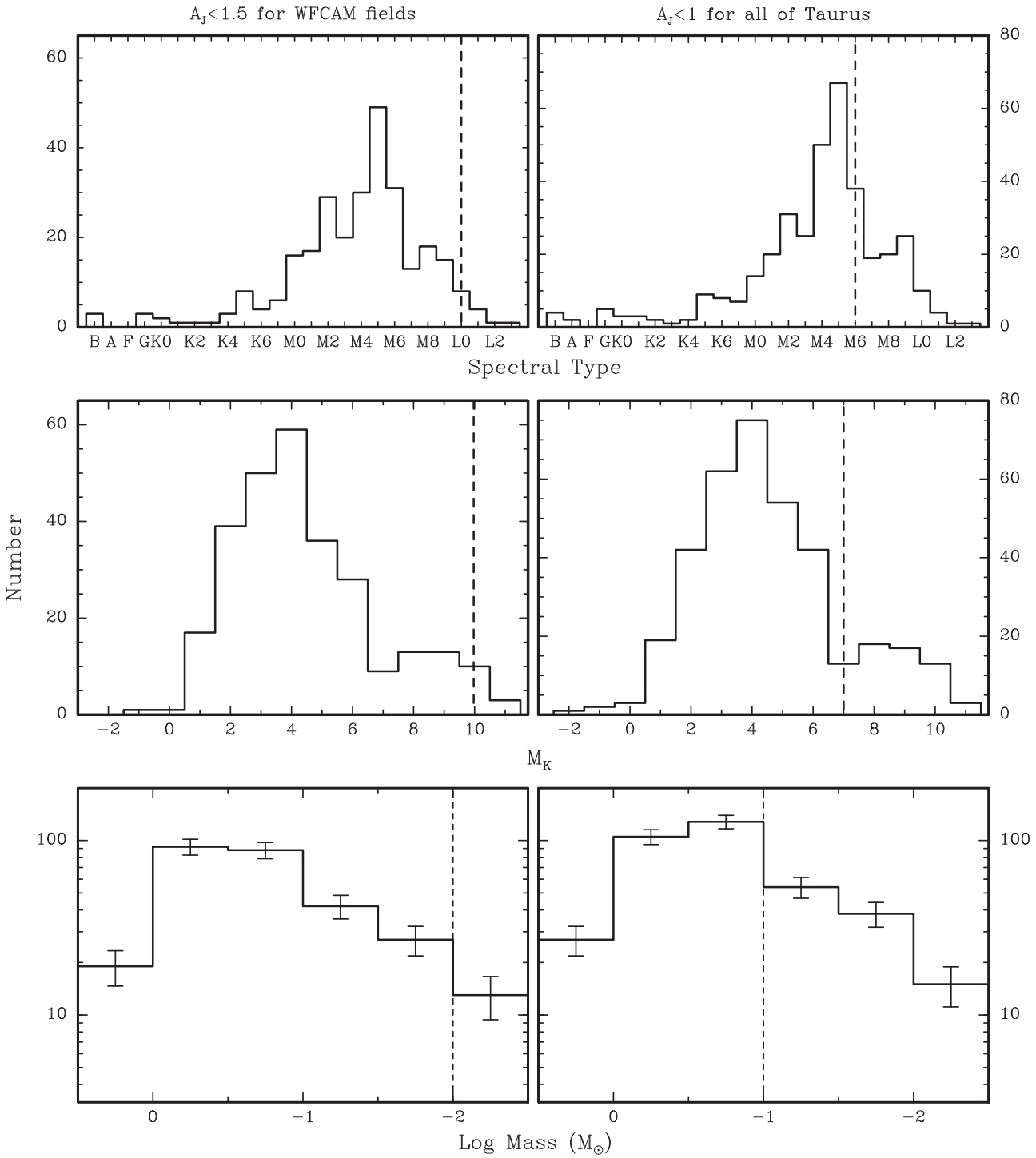

Figure 22. Distributions of spectral types, extinction-corrected M_K, and masses for known members of Taurus with $A_J < 1.5$ for the WFCAM fields from Figure 11 (left) and for members with $A_J < 1$ in the entire region (right). Members were placed in bins of mass based on their spectral types in the same way done in Figure 19. The completeness limits for the samples are indicated (dashed lines).

members of Taurus, which brings the total number of known members in our census to 519. Our survey has doubled the number of known members at ⩾M9 and has uncovered the faintest known members in M_K, which should have masses extending down to ∼3–10 $M_{\rm Jup}$ for ages of 1–10 Myr (Burrows et al. 1997; Chabrier et al. 2000).

According to data from *Gaia* DR2, our census of Taurus should be nearly complete for spectral types earlier than M6–M7 at $A_J < 1$ across the entire cloud complex (Luhman 2018). Meanwhile, we have demonstrated that the census should be complete for extinction-corrected magnitudes of $K < 15.7$ at $A_J < 1.5$ within a large field that encompasses ∼72% of the known members. That magnitude limit corresponds to ∼5–13 $M_{\rm Jup}$ for ages of 1–10 Myr. For the known members within that field and extinction limit, we have used distributions of spectral types and M_K as observational proxies for the IMF. Those distributions

remain roughly constant at substellar masses down to the completeness limit and thus show no sign of a decline toward a low-mass cutoff.

We have used mid-IR photometry from *Spitzer* and *WISE* to search for evidence of circumstellar disks among the new members from our survey, as well as the few members adopted by Luhman (2018) that were not examined for disks by Esplin & Luhman (2017) or earlier studies. By combining those results with disk classifications for all other members in our census (Luhman et al. 2010; Esplin et al. 2014; Esplin & Luhman 2017), we have derived a disk fraction of ∼0.7 and 0.4 for spectral types of ⩽M3.5 and >M3.5, respectively, which is slightly lower than previous measurements based on less complete catalogs of members (Luhman et al. 2010).

K.L. acknowledges support from NASA grant 80NSSC18 K0444. The UKIRT data were obtained through program U/17B/UA05. UKIRT is owned by the University of Hawaii (UH) and operated by the UH Institute for Astronomy. When the data reported here were acquired, UKIRT was supported by NASA and operated under an agreement among the University of Hawaii, the University of Arizona, and the Lockheed Martin Advanced Technology Center; operations were enabled through the cooperation of the East Asian Observatory. This work has made use of data from the European Space Agency (ESA) mission *Gaia* (https://www.cosmos.esa.int/gaia), processed by the *Gaia* Data Processing and Analysis Consortium (DPAC; https://www.cosmos.esa.int/web/gaia/dpac/consortium). Funding for the DPAC has been provided by national institutions, in particular the institutions participating in the *Gaia* Multilateral Agreement. The Gemini data were obtained through programs GN-2017B-Q-8, GN-2018B-Q-114, GN-2018B-FT-205, and GN-2018B-FT-207. Gemini is operated by the Association of Universities for Research in Astronomy, Inc., under a cooperative agreement with the NSF on behalf of the Gemini partnership: the National Science Foundation (United States), the National Research Council (Canada), CONICYT (Chile), Ministerio de Ciencia, Tecnología e Innovación Productiva (Argentina), and Ministério da Ciência, Tecnologia e Inovação (Brazil). The IRTF is operated by the University of Hawaii under contract NNH14CK55B with NASA. The MMT Observatory is a joint facility of the University of Arizona and the Smithsonian Institution. LRS2 was developed and funded by the University of Texas at Austin McDonald Observatory and Department of Astronomy and by Pennsylvania State University. We thank the Leibniz-Institut für Astrophysik Potsdam (AIP) and the Institut fur Astrophysik Göttingen (IAG) for their contributions to the construction of the integral field units. The HET is a joint project of the University of Texas at Austin, the Pennsylvania State University, Stanford University, Ludwig-Maximillians-Universität München, and Georg-August-Universität Göttingen and is named in honor of its principal benefactors, William P. Hobby and Robert E. Eberly. The LAMOST data were obtained with the Guoshoujing Telescope, which is a National Major Scientific Project built by the Chinese Academy of Sciences. Funding for the project has been provided by the National Development and Reform Commission. LAMOST is operated and managed by the National Astronomical Observatories, Chinese Academy of Sciences. WIRCAM is a joint project of CFHT, Taiwan, Korea, Canada, France, and the Canada–France–Hawaii Telescope (CFHT), which is operated by the National Research Council (NRC) of Canada, the Institute National des Sciences de l'Univers of the Centre National de la Recherche Scientifique of France, and the University of Hawaii. The *Spitzer Space Telescope* and the IPAC Infrared Science Archive (IRSA) are operated by JPL and Caltech under contract with NASA. 2MASS is a joint project of the University of Massachusetts and the Infrared Processing and Analysis Center (IPAC) at Caltech, funded by NASA and the NSF. Funding for SDSS has been provided by the Alfred P. Sloan Foundation, the Participating Institutions, the NSF, the U.S. Department of Energy, NASA, the Japanese Monbukagakusho, the Max Planck Society, and the Higher Education Funding Council for England. The SDSS website is http://www.sdss.org/. The SDSS is managed by the Astrophysical Research Consortium for the Participating Institutions. The Participating Institutions are the American Museum of Natural History, Astrophysical Institute Potsdam, University of Basel, University of Cambridge, Case Western Reserve University, The University of Chicago, Drexel University, Fermilab, the Institute for Advanced Study, the Japan Participation Group, Johns Hopkins University, the Joint Institute for Nuclear Astrophysics, the Kavli Institute for Particle Astrophysics and Cosmology, the Korean Scientist Group, the Chinese Academy of Sciences, Los Alamos National Laboratory, the Max-Planck-Institute for Astronomy, the Max-Planck-Institute for Astrophysics, New Mexico State University, The Ohio State University, University of Pittsburgh, University of Portsmouth, Princeton University, the United States Naval Observatory, and the University of Washington. PS1 and its public science archive have been made possible through contributions by the Institute for Astronomy, the University of Hawaii, the Pan-STARRS Project Office, the Max-Planck Society and its participating institutes, the Max Planck Institute for Astronomy, Heidelberg, and the Max Planck Institute for Extraterrestrial Physics, Garching, Johns Hopkins University, Durham University, the University of Edinburgh, the Queen's University Belfast, the Harvard-Smithsonian Center for Astrophysics, the Las Cumbres Observatory Global Telescope Network Incorporated, the National Central University of Taiwan, the Space Telescope Science Institute, the National Aeronautics and Space Administration under grant NNX08AR22G issued through the Planetary Science Division of the NASA Science Mission Directorate, NSF grant AST-1238877, the University of Maryland, Eotvos Lorand University (ELTE), the Los Alamos National Laboratory, and the Gordon and Betty Moore Foundation. The Center for Exoplanets and Habitable Worlds is supported by the Pennsylvania State University, the Eberly College of Science, and the Pennsylvania Space Grant Consortium.

Facilities: UKIRT (WFCAM), MMT (Red Channel, MMIRS), Gemini:North (GMOS, GNIRS), CFHT (WIRCam), IRTF (SpeX), *Spitzer* (IRAC), HET (LRS2).

Appendix
Comments on Individual Sources

Gaia 164475467659453056 and *Gaia* 164475467657712256 (2MASS J04161407+2758275 N and S) comprise a pair with a separation of 0.″9 (Section 4). The first component has a discrepant parallax for Taurus membership (Figure 2), but its astrometry is probably unreliable based on its large RUWE (5.1) and the *Gaia* data for the second component, which support membership. LAMOST provides a spectrum of the combined light from the pair. Since the components have similar G magnitudes, we have assigned the resulting spectral classification to both of them. In the diagram of M_J versus spectral type in

Figure 2, only the second component is plotted, and that is done using half of the *J*-band flux from 2MASS.

2MASS J04053214+2733139, 2MASS J04064263+2902014, 2MASS J04212650+2952476, and 2MASS J04422776 +2939448 are not within any of the fields marked in Figure 1 and shown in Figures 2–10. The data for those stars are included in the photometric and kinematic diagrams of neighboring fields, corresponding to Figures 2, 3, and 9, respectively.

2MASS J04334298+2235566 is intermediate between the red and blue populations in terms of parallax (Figure 6). We have assigned it to the red group based on better agreement in proper motion.

The parallax and proper motion of 2MASS J04343664 +1836255 are inconsistent with membership, but those data are probably unreliable (RUWE = 8.2). In Figure 8, the star is beyond the boundaries of the parallax diagram, labeled in the proper motion diagram, and omitted from M_J versus spectral type.

The previously known members 2MASS J05080816 +2427150 A and B comprise a 0.″94 pair. The former lacks measurements of proper motion and parallax from *Gaia*, likely due to a poor astrometric fit (RUWE = 71). The secondary has a discrepant proper motion (Figure 10), which is probably unreliable (RUWE = 3.0).

As mentioned in Section 2, we have adopted 2MASS J04282999+2358482 as a Taurus member, which was classified as a young M8 dwarf by Gizis et al. (1999). Using our classification methods, we have measured a spectral type of M9.25 from the optical spectrum in that study.

Because of its moderately low S/N, the spectrum of UGCS J042443.77+270453.4 can be matched with either a young early L dwarf or an old mid-L dwarf. We measure a proper motion of (μ_α, μ_δ = 2.9 ± 1.3, −16.8 ± 5.3 mas yr^{-1}) from the data in Section 3.3, which is consistent with membership (Figure 13). Its small distance from a known member (3′) is also suggestive of membership. We tentatively adopt it as a member, but a spectrum with higher S/N would be useful for confirming its youth.

2MASS J04575235+2954072 exhibits evidence of youth in the form of Li absorption, but the feature is weaker than in most K/M Taurus members (0.2 Å vs. ≳0.4 Å). The star agrees well with its neighboring known members in terms of parallax, proper motion, and the age implied by M_J versus spectral type, so we adopt it as a member.

The LAMOST spectrum of 2MASS J04053214+2733139 shows Li absorption (0.4 Å), while the resolution of the spectrum from Red Channel is too low for a useful constraint on the feature. The star's parallax and proper motion closely match those of the red group in Figure 2, but given the large distance from that group (∼2°), we consider its membership to be tentative.

2MASS J04404677+1928033 and 2MASS J05080636 +3026233 have moderately weak Li (0.3 Å) for Taurus members and share similar kinematics to the blue and cyan groups in Figures 8 and 9, respectively. We adopt both stars as members, but the membership of the former is considered tentative because of its large distance from other members.

2MASS J04474012+2850409, 2MASS J04491437+2934354, and 2MASS J04505864+2852218 are among the *Gaia* candidates from Luhman (2018) and are located near each other in the field in Figure 9, where they are plotted as crosses. The second star has Li absorption comparable to that of Taurus members (0.48 Å), while the other stars have unusually weak Li for Taurus (0.18 Å). The three stars exhibit nearly identical parallaxes, proper motion offsets, and ages (Figure 9), indicating that they are members of a coeval, comoving group. The weak Li lines for two of the stars are consistent with the ages implied by the diagram of M_J versus spectral type (10–20 Myr). Their parallaxes and motions are distinct from those of the Taurus populations, so we classify them as nonmembers. We note that a few of the known members in Figure 9 have proper motion offsets that appear to be as discrepant as those of the three stars in the preceding discussion (e.g., the stars at the top and bottom of the clump of members). All of those outliers have RUWE ≳ 1.4, so their discrepant offsets may be due to poor astrometric fits.

2MASS J04404936+2732166 is plotted as the cyan open square in Figure 5. In terms of parallax and proper motion offset, it matches more closely with the cyan population in the neighboring field in Figure 9 than the red population in Figure 5, although there remains a modest difference in proper motion offsets. Its gravity-sensitive spectral features and position in the diagram of M_J versus spectral type are consistent with the age of that cyan population, so we tentatively assign membership to it.

2MASS J04292852+2106069 is located between the fields for Figures 6 and 8. The presence of Li absorption indicates youth. Although it was identified as a candidate member based on its parallax and proper motion (Luhman 2018), it is near the thresholds for selection in both parameters. Given its remote location and modest discrepancy in parallax and proper motion relative to other members, we treat its membership as undetermined.

2MASS J04443916+2224417 shows evidence of moderate youth in its weak Li absorption (0.15 Å), but it does not agree well with any of the groups of known members in terms of its parallax and proper motion, so we classify it as a nonmember.

2MASS J05023985+2459337 and 2MASS J05010116 +2501413 are marked with crosses in Figure 10. Luhman (2018) adopted the former as a member of Taurus but noted that it exhibits a discrepant proper motion offset relative to Taurus members in its field. The second star was selected by Luhman (2018) as a candidate member using *Gaia* astrometry, appearing near the threshold for selection in proper motion offset. The two stars have similar proper motion offsets, parallaxes, and ages (Figure 10), indicating that they are likely associated with each other. We classify them as nonmembers based on their discrepant motions relative to the Taurus members in their field.

2MASS J04195030+2926477 exhibits signatures of youth in its optical and near-IR spectra. Its *Gaia* astrometry is inconsistent with membership, but those data may not be reliable (RUWE = 1.95). Given its remote location relative to the Taurus groups (slightly beyond the northern boundary of Figure 3), youth alone is insufficient evidence of membership, so we treat it as a nonmember.

Luhman (2018) noted that T Tau differs from the other members of its red population in terms of its proper motion offset (Figure 8). Its value of RUWE is somewhat high (1.7; Figure 14), so it may have a poor astrometric fit, which could explain this discrepancy.

In Section 5.1, we classified seven of our candidate members of Taurus using IR spectra that were publicly available from Gemini programs GN-2017A-Q-81, GN-2017B-Q-19, and GN-2017B-Q-35. Although they were not selected as candidates in our analysis, we have examined the spectra of the remaining 38 objects from those programs. One of the targets is a previously known member

of Taurus, UGCS J043354.07+225119.1 (Esplin & Luhman 2017). We classify one source as a galaxy and 34 sources as field stars. The remaining two objects, 2MASS J04390237+2332133 and UGCS 044344.10+261749.9, appear to be young and have spectral types of M9–L1 based on comparison to the young standards from Luhman et al. (2017). However, both of them fall below the sequence of known members in multiple CMDs. Young stars that are seen in scattered light can appear underluminous for their colors, but these two objects do not show evidence of circumstellar disks in their mid-IR photometry. Instead, they may be members of the populations of intermediate-age stars ($\gtrsim$10 Myr) in the direction of Taurus that are unrelated to the cloud complex and its newly formed stars (Luhman 2018). We measure proper motions of (10.6 ± 2.4, -29.0 ± 5.3 mas yr^{-1}) for 2MASS J04390237+2332133 and (16.4 ± 7.4, -45.1 ± 2.9 mas yr^{-1}) for UGCS 044344.10+261749.9. The former is consistent with membership, while the latter is not. Given its proper motion and proximity to known members, 2MASS J04390237+2332133 seems more likely to be a member, but we treat both objects as nonmembers based on their underluminous nature.

ORCID iDs

T. L. Esplin https://orcid.org/0000-0001-9223-9091
K. L. Luhman https://orcid.org/0000-0003-2822-2951

References

Albareti, F. D., Allende Prieto, C., Almeida, A., et al. 2017, ApJS, 233, 25
André, P., Ward-Thompson, D., & Barsony, M. 1993, ApJ, 406, 122
Baraffe, I., Chabrier, G., Allard, F., & Hauschildt, P. H. 1998, A&A, 337, 403
Baraffe, I., Hormeier, D., Allard, F., & Chabrier, G. 2015, A&A, 577, 42
Basri, G., Martín, E. L., & Bertout, C. 1991, A&A, 252, 625
Beck, T. L. 2007, AJ, 133, 1673
Best, W. M. J., Liu, M. C., Dupuy, T. J., & Magnier, E. A. 2017, ApJL, 843, L4
Briceño, C., Hartmann, L., Stauffer, J. R., & Martín, E. 1998, AJ, 115, 2074
Burrows, A., Marley, M., Hubbard, W. B., et al. 1997, ApJ, 491, 856
Calvet, N., Muzerolle, J., Briceño, C., et al. 2004, AJ, 128, 1294
Casali, M., Lunney, D., Henry, D., et al. 2001, ASPC, 232, 357
Chabrier, G. 2005, in The Initial Mass Function 50 Years Later, ed. E. Corbelli & F. Palle (Potsdam: Springer), 41
Chabrier, G., Baraffe, I., Allard, F., & Hauschildt, P. 2000, ApJ, 542, 464
Chambers, K. C., Magnier, E. A., Metcalfe, N., et al. 2016, arXiv:1612.05560
Chonis, T. S., Hill, G. J., Lee, H., et al. 2014, Proc. SPIE, 9147, 91470A
Chonis, T. S., Hill, G. J., Lee, H., et al. 2016, Proc. SPIE, 9908, 99084C
Cui, X., Zhao, Y., Chu, Y., et al. 2012, RAA, 12, 1197
Cushing, M. C., Rayner, J. T., & Vacca, W. D. 2005, ApJ, 623, 1115
Cushing, M. C., Vacca, W. D., & Rayner, J. T. 2004, PASP, 116, 362
Cutri, R. M., Skrutskie, M. F., van Dyk, S., et al. 2013, yCat, 2246, 0
Da Rio, N., Robberto, M., Hillenbrand, L. A., Henning, T., & Stassun, K. G. 2012, ApJ, 748, 14
Davis, B. D., Ciardullo, R., Jacoby, G. H., Feldmeier, J. J., & Indahl, B. L. 2018, ApJ, 863, 189
de Bruijne, J. H. J. 2012, Ap&SS, 341, 31
DeWarf, L. E., Sepinsky, J. F., Guinan, E. F., et al. 2003, ApJ, 590, 357
Dobashi, K., Uehara, H., Kandori, R., et al. 2005, PASJ, 57, 1
Dye, S., Lawrence, A., Read, M. A., et al. 2018, MNRAS, 473, 5113
Elias, J. H., Joyce, R. R., Liang, M., et al. 2006, Proc. SPIE, 6269, 62694C
Espaillat, C., Ingleby, L., Hernandez, J., et al. 2012, ApJ, 747, 103
Esplin, T. L., & Luhman, K. L. 2017, AJ, 154, 134
Esplin, T. L., Luhman, K. L., Faherty, J. K., Mamajek, E. E., & Bochanski, J. J. 2017, AJ, 154, 46
Esplin, T. L., Luhman, K. L., & Mamajek, E. E. 2014, ApJ, 784, 126
Esplin, T. L., Luhman, K. L., Miller, E. B., & Mamajek, E. E. 2018, AJ, 156, 75
Fazio, G. G., Hora, J. L., Allen, L. E., et al. 2004, ApJS, 154, 10
Feiden, G. A. 2016, A&A, 593, A99
Filippazzo, J. C., Rice, E. L., Faherty, J., et al. 2015, ApJ, 810, 158
Finkbeiner, D. P., Padmanabhan, N., Schlegel, D. J., et al. 2004, AJ, 128, 2577
Flewelling, H. A., Magnier, E. A., Chambers, K. C., et al. 2016, arXiv:1612.05243
Gaia Collaboration, Brown, A. G. A., Vallenari, A., et al. 2016a, A&A, 595, A2
Gaia Collaboration, Brown, A. G. A., Vallenari, A., et al. 2018, A&A, 616, A1
Gaia Collaboration, Prusti, T., de Bruijne, J. H. J., et al. 2016b, A&A, 595, A1
Galli, P. A. B., Loinard, L., Ortiz-Léon, G. N., et al. 2018, ApJ, 859, 33
Gizis, J. E., Reid, I. N., & Monet, D. G. 1999, AJ, 118, 997
Greene, T. P., Wilking, B. A., André, P., Young, E. T., & Lada, C. J. 1994, ApJ, 434, 614
Hambly, N. C., Collins, R. S., Cross, N. J. G., et al. 2008, MNRAS, 384, 637
Henry, T. J., Kirkpatrick, J. D., & Simons, D. A. 1994, AJ, 108, 1437
Hernández, J., Hartmann, L., Megeath, T., et al. 2007, ApJ, 662, 1067
Hillenbrand, L. A., Hoffer, A. S., & Herczeg, G. J. 2013, AJ, 146, 85
Hook, I., Jørgensen, I., Allington-Smith, J. R., et al. 2004, PASP, 116, 425
Indebetouw, R., Mathis, J. S., Babler, B. L., et al. 2005, ApJ, 619, 931
Irwin, M. J., Lewis, J., Hodgkin, S., et al. 2004, Proc. SPIE, 5493, 411
Kaiser, N., Aussel, H., Burke, B. E., et al. 2002, Proc. SPIE, 4836, 154
Kaiser, N., Burgett, W., Chambers, K., et al. 2010, Proc. SPIE, 7733, 77330E
Kellogg, K., Metchev, S., Geißler, K., et al. 2015, AJ, 150, 182
Kenyon, S. J., & Bromley, B. C. 2005, AJ, 130, 269
Kenyon, S. J., Gómez, M., & Whitney, B. A. 2008, in Handbook of Star-forming Regions, Vol. 1: The Northern Sky, ed. B. Reipurth (San Fransisco, CA: ASP), 405
Kirkpatrick, J. D., Henry, T. J., & Irwin, M. J. 1997, AJ, 113, 1421
Kirkpatrick, J. D., Henry, T. J., & McCarthy, D. W. 1991, ApJS, 77, 417
Kirkpatrick, J. D., Martin, E. C., Smart, R. L., et al. 2019, ApJS, 240, 19
Kraus, A. L., Herczeg, G. J., Rizzuto, A. C., et al. 2017, ApJ, 838, 150
Lada, C. J. 1987, in IAU Symp. 115, Star-forming Regions, ed. M. Peimbert & J. Jugaku (Dordrecht: Reidel), 1
Lada, C. J., & Wilking, B. A. 1984, ApJ, 287, 610
Lawrence, A., Warren, S. J., Almaini, O., et al. 2007, MNRAS, 379, 1599
Lindegren, L. 2018, Re-normalising the Astrometric Chi-square in Gaia, DR2 GAIA-C3-TN-LU-LL-124-01, http://www.rssd.esa.int/doc_fetch.php?id=3757412
Liu, M. C., Magnier, E. A., Deacon, N. R., et al. 2013, ApJL, 777, L20
Lodieu, N., Zapatero Osorio, M. R., Béjar, V. J. S., & Peña Ramírez, K. 2018, MNRAS, 473, 2020
Lucas, P. W., Roche, P. F., Allard, F., & Hauschildt, P. H. 2001, MNRAS, 326, 695
Luhman, K. L. 1999a, ApJ, 525, 466
Luhman, K. L. 1999b, ApJ, 544, 1044
Luhman, K. L. 2018, AJ, 156, 271
Luhman, K. L., Allen, P. R., Espaillat, C., Hartmann, L., & Calvet, N. 2010, ApJS, 186, 111
Luhman, K. L., Briceño, C., Stauffer, J. R., et al. 2003, ApJ, 590, 348
Luhman, K. L., Esplin, T. E., & Loutrel, N. P. 2016, ApJ, 827, 52
Luhman, K. L., Liebert, J., & Rieke, G. H. 1997, ApJL, 489, L165
Luhman, K. L., Mamajek, E. E., Shukla, S. J., & Loutrel, N. P. 2017, AJ, 153, 46
Magazzú, A., Rebolo, R., & Pavlenko, Ya. V. 1992, ApJ, 392, 159
Martín, E. L., Rebolo, R., Magazzú, A., & Pavlenko, Ya. V. 1994, A&A, 282, 503
Martín, E. L., Rebolo, R., & Zapatero Osorio, M. R. 1996, ApJ, 469, 706
McLeod, B., Fabricant, D., Nystrom, G., et al. 2012, PASP, 124, 1318
Meyer, M. R., Calvet, N., & Hillenbrand, L. A. 1997, AJ, 114, 288
Palla, F., & Stahler, S. W. 2000, ApJ, 540, 255
Pecaut, M. J., Mamajek, E. E., & Bubar, E. J. 2012, ApJ, 746, 154
Perryman, M. A. C., de Boer, K. S., Gilmore, G., et al. 2001, A&A, 369, 339
Rayner, J. T., Cushing, M. C., & Vacca, W. D. 2009, ApJS, 185, 289
Rayner, J. T., Toomey, D. W., Onaka, P. M., et al. 2003, PASP, 115, 362
Rieke, G. H., Su, K. Y. L., Stansberry, J. A., et al. 2005, ApJ, 620, 1010
Rieke, G. H., Young, E. T., Engelbracht, C. W., et al. 2004, ApJS, 154, 25
Schlafly, E. F., Meisner, A. M., Stutz, A. M., et al. 2016, ApJ, 821, 78
Schmidt, G. G., Weymann, R. J., & Foltz, C. B. 1989, PASP, 101, 713
Schneider, A. C., Windsor, J., Cushing, M. C., Kirkpatrick, J. D., & Wright, E. L. 2016, ApJL, 822, L1
Skrutskie, M., Cutri, R. M., Stiening, R., et al. 2006, AJ, 131, 1163
Strom, K. M., & Strom, S. E. 1994, ApJ, 424, 237
Vacca, W. D., Cushing, M. C., & Rayner, J. T. 2003, PASP, 115, 389
Werner, M. W., Roellig, T. L., Low, F. J., et al. 2004, ApJS, 154, 1
White, R. J., & Ghez, A. M. 2001, ApJ, 556, 265
Wright, E. L., Eisenhardt, P. R., Mainzer, A. K., et al. 2010, AJ, 140, 1868
Xue, M., Jiang, B. W., Liu, J., et al. 2016, ApJS, 224, 23
York, D. G., Adelman, J., Anderson, J. E., et al. 2000, AJ, 120, 1579
Zapatero Osorio, M. R., Béjar, V. J. S., & Peña Ramírez, K. 2017, ApJ, 842, 65
Zhang, Z., Liu, M. C., Best, W. M. J., et al. 2018, ApJ, 858, 41
Zhao, G., Zhao, Y. H., Chu, Y. Q., Jing, Y. P., & Deng, L. C. 2012, RAA, 12, 723